Two-dimensional Cu-based Metal–Organic Frameworks as electrochemical catalysts for CO_2 reduction

Yu Bi

to obtain the degree Master of Science, in Materials Science and Engineering, at the Delft University of Technology, to be defended publicly on 24th August, 2022

Student number	**5238986**	
Thesis committee	**Dr. P. Taheri**	**TU Delft**
	Dr. M. Ramdin (P&E)	**TU Delft**
	Dr. P. Gonugunta	**TU Delft**
	Dr. M. Soleimani	**TU Delft**
	K. Roohi MSc	**TU Delft**
Daily supervisors	**Dr. P. Taheri**	**TU Delft**
	K. Roohi MSc	**TU Delft**

Abstract

In the past decades, the rapid development of industry and economy leads to heavy dependency on fossil fuels which causes increasing concentration of CO_2 in atmosphere. Now, excessive CO_2 emission has accelerated global warming and caused a series of irreversible environmental problems. To address this problem, electrochemical conversion of CO_2 is considered one of the most promising strategies due to its mild operating conditions, utilization of renewable sources of energy and controllability of the process. However, CO_2 reduction faces many difficulties which requires active catalysts to achieve effective conversion. Among all the catalysts, Copper (Cu)-based Metal-Organic Frameworks (MOFs) become very attracting candidates due to their high porosity, tunable structure and special properties to convert CO_2 into various hydrocarbons. In particular, two-dimensional (2D) Cu-MOFs can further improve the electrical conductivity and catalytic activity. In this study, three types of Cu-based MOFs are studied as catalysts for CO_2 reduction reaction (CO_2RR). Among them, Cu-BTC is a conventional 3D MOF, Cu-HAB and Cu-HHTP belong to the category of conventional 2D MOFs. In particular, Cu-HAB has not been used as catalyst for CO_2 reduction before. To investigate their catalytic performance for CO_2 reduction, the surface morphologies and bond structures were first characterized by Scanning Electron Microscopy (SEM), Energy Dispersive Spectroscopy (EDS) and Fourier-transform infrared spectroscopy (FTIR). Then Linear sweep voltammetry (LSV), Cyclic Voltammetry (CV), Electrochemical Impedance Spectroscopy (EIS) and Chronoamperometry (CA) were used to examine the electrochemical performance and stability of them. In the last, the product selectivity of Cu-HAB and Cu-HHTP was tested using Gas Chromatography (GC) and Nuclear Magnetic Resonance (NMR). From the results, 2D MOFs show higher catalytic activity, capacitance and conductivity which suggest 2D structure is beneficial for catalytic process. Especially Cu-HAB shows the best conductivity and catalytic activity due to presence of Cu-N_4 coordination in the MOF structure as well as smaller particles. But from the point of view of product selectivity, Cu-HHTP performs better than Cu-HAB which may indicate Cu-O_4 sites can better engage with CO_2 molecule and transfer it to other product.

Acknowledges

During the whole project, I have received a lot of help from different people. I feel very lucky to enter this group and meet so many excellent people here. I'd like to take this opportunity to express my gratitude.
First, I'd like to thank my supervisors Dr. Peyman Taheri for the guidance and support during the whole project. And I have to express special thanks to my daily supervisor Khatereh Roohi for giving me a lot of help when I meet difficulties in the experiments, guiding me when I was confused, spending a lot of time reading and giving me feedback to my thesis. I'm so lucky to have you as my daily supervisor.
I also need to thank Agnieszka Kooijman for teaching me with lab work and helping me order the materials. Besides, I'd like to say a word of thanks to Prasad Gonugunta, Eszter Mádai, Mohammad Soleimani, Jasper Coppen, Songyan Liu and all other people in the group. Thank you for all the advice and conversation we shared!
And thank Nandalal Girichandran for helping me with NMR measurements.
In the last, I have to say thanks to my friends and family. Thanks a lot for supporting me and listening my all the worries. Thank you for your continued company.

Yu Bi
Delft, August 2022

Contents

Abstract III
Acknowledge IV
List of Figures VII
List of Tables IX
Acronyms X
1 Introduction 1
1.1 Background 1
1.2 Objectives 2
1.3 Approaches 2
1.4 Structure of the thesis 2
2 Theorical Study 3
2.1 Fundamentals of electrocatalytic CO_2RR 3
2.2 Performance indicators for electrocatalytic CO_2RR 5
2.2.1 Faraday efficiency 5
2.2.2 Overpotential 6
2.2.3 Current density 6
2.3 Common Electrocatalysts for CO_2RR 6
2.3.1 Metallic Catalysts 6
2.3.2 Carbon-based Catalysts 7
2.3.3 State of the art 2D transition metal dichalcogenides 8
2.3.4 Metal-organic framework 9
2.4 Cu-based MOFs for CO_2RR 11
2.4.1 Cu-BTC MOF 11
2.4.2 Cu-HAB MOF 12
2.4.3 Cu-HHTP MOF 12
3 Experimental Section 15
3.1 Synthesis of Cu-HAB 15
3.2 Synthesis of Cu-HAB 15
3.3 Preparation of working electrode 16

3.4 Characterization techniques 17
3.4.1 SEM 17
3.4.2 EDS 17
3.4.3 FTIR 17
3.5 Electrochemical measurements 19
3.5.1 Cyclic Voltammetry 19
3.5.2 Linear Sweep Voltammetry 20
3.5.3 Electrochemical Impedance Spectroscopy 20
3.5.4 Chronoamperometry 21
3.6 Product analysis 21
3.6.1 Gas Chromography 22
3.6.2 Nuclear Magnetic Resonance 23
4 Results and Discussion 25
4.1 Surface characterization 25
4.1.1 SEM and EDS 25
4.1.2 FTIR 29
4.2 Electrochemical measurements 32
4.2.1 LSV and CV results 32
4.2.2 EIS results 35
4.2.3 CA results 35
4.3 Product analysis 36
4.3.1 GC 36
4.3.2 NMR 38
5 Conclusion 39
6 Future Outlook 41
Appendix 42
Reference 44

List of figures

Figure 1 Schematic illustration of CO_2RR in a three-electrodes system 4
Figure 2 Schematic illustration of electrical double layer at cathode 5
Figure 3 Schematic diagram of the mechanism of CO_2RR on metal surfaces 7
Figure 4 a) basic structure of TMDs. b) trigonal prismatic and c) octahedral coordination of TMDs from axis view and d) side view. e) schematic illustration of TMDs catalytic reaction 8
Figure 5 Typical organic ligands and the relevant 2D c-MOFs. (a) Benzene-based, (b) benzoquinone/benzene-based, (c) triphenylene-based, (d) coronene-based, (e) phthalocyanine-based, and (f) dibenzo[g,p]chrysene-based ligand monomers 10
Figure 6 a) LSV results of Cu-THQ NFs of different particle sizes for electrochemical CO_2 reduction in 1 m choline chloride and 1 m KOH at 50 mV/s. b) DEMS results of Cu-THQ NFs for CO and H_2 production during LSV experiment with scan rate of 1 mV/s 10
Figure 7 The chemical structure of Cu-BTC 11
Figure 8 Structure of Cu-HAB, M represents metal atoms (Cu) 12
Figure 9 The crystal structure of Cu-HHTP 13
Figure 10 A schematic diagram of the synthesizing process for Cu-HAB 16
Figure 11 Schematic diagram of FTIR 18
Figure 12 Experimental setup for electrochemical measurements 19
Figure 13 Schemes of redox reaction on the surface and equivalent circuit 20
Figure 14 “Nyquist Plot" according to the equivalent circuit 21
Figure 15 Simple schematic of GC system 22
Figure 16 Electrochemical flow cell of GC measurements 23
Figure 17 Schematic presentation of a typical NMR 23
Figure 18 SEM images of Cu-BTC sample. The scale bar corresponds to (a) 500 µm, (b) 100 µm, (c) 50 µm, (d) 10 µm 26
Figure 19 EDS spectrum of Cu-BTC sample 26
Figure 20 EDS mapping of element distribution in pyramidal shaped crystal 27
Figure 21 SEM images of Cu-HAB sample. The scale bar corresponds to 200 µm for (a), 100 µm for (b), 50 µm for (c) and 10 µm for (d) 27
Figure 22 EDS spectrum of Cu-HAB sample 28
Figure 23 SEM images of Cu-HHTP sample. The scale bar corresponds to 200 µm for (a), 100 µm for (b), 50 µm for (c) and 10 µm for (d) 29
Figure 24 EDS spectrum of Cu-HHTP sample 29
Figure 25 FTIR spectrum of Cu-BTC sample 30
Figure 26 FTIR spectrum of Cu-HAB sample 30
Figure 27 FTIR spectrum of Cu-HHTP sample 31
Figure 28 The a) LSV and b) CV curves of Cu-BTC sample in CO_2 and N_2 saturated electrolyte 32

Figure 29 The a) LSV and b) CV curves of Cu-HAB sample in CO_2 and N_2 saturated electrolyte 33
Figure 30 The a) LSV and b) CV curves of Cu-HHTP sample in CO_2 and N_2 saturated electrolyte 34
Figure 31 The a) LSV and b) CV curves of Cu-BTC, Cu-HAB and Cu-HHTP samples in CO_2 saturated electrolyte. 34
Figure 32 The EIS results for a) Cu-BTC, b) Cu-HAB, c) Cu-HHTP, d) overall for all three MOFs 35
Figure 33 The CA results for Cu-HAB, Cu-BTC, Cu-HHTP samples at -1.6V vs Ag/AgCl 36
Figure 34 The average FEs calculated a) Cu-HAB, b) Cu-HHTP samples and c) gas products of two MOFs 37
Figure 35 The average FEs of liquid products fora) Cu-HAB and b) Cu-HHTP samples 38
Figure A.1 Calibration plots for a) H_2, b) CH_4, c) C_2H_4, d) CO 42
Figure A.2 FE-time plot of a) H_2, b) CH_4, c) C_2H_4 product for Cu-HAB sample 43
Figure A.3 FE-time plot of a) H_2, b) CH_4, c) C_2H_4 product for Cu-HHTP sample 43

List of tables

Table 1 Common CO2RR half-reactions and corresponding potentials in aqueous solution (1.0 atm, 25 °C, PH=7, and 1.0 M concentration of other solutes) 3

Table 2 elemental composite of Cu-BTC 27

Table 3 elemental composite of Cu-HAB 28

Table 4 elemental composite of Cu-HHTP 29

Acronyms

2D two-dimensional
3D three-dimensional
AM active material
CA Chronoamperometry
CB carbon black
CO_2RR CO_2 reduction reaction
CNTs carbon nanotubes
CV Cyclic Voltammetry
EDL electrical double layer
EDS Energy Dispersive Spectroscopy
EIS Electrochemical Impedance Spectroscopy
FE faraday efficiency
FID flame ionization detector
FTIR Fourier-transform infrared spectroscopy
GC Gas Chromatography
HER hydrogen evolution reaction
IHP Inner Helmholtz plane
IPA isopropanol
LSV Linear sweep voltammetry
MOFs Metal-Organic Frameworks
NCNTs nitrogen-doped carbon nanotubes
NMR Nuclear Magnetic Resonance
OER oxygen evolution reaction
OHP Outer Helmholtz plane
PVA Polyvinyl alcohol
RHE reversible hydrogen electrode
SCE saturated calomel electrode
SEM Scanning Electron Microscopy
SHE hydrogen reference electrode
TCD thermal conductivity detectors
TMDs transition metal chalcogenides
TMOs transition metal dioxides

1

Introduction

1.1 Background

The rapid development of industry and economy and frequent use of fossil fuels have led to the high concentration of CO_2 in atmosphere. Now, excessive CO_2 emission has become a serious problem. Several strategies have been developed to overcome this problem. In this regard, utilization of porous materials as physical or chemical adsorbents of CO_2 can be mentioned as an example. However, CO_2 capture costs a lot of energy and money and its limited capacity of capturing and adsorption further reduces its applicability [1]. On the other hand, CO_2 conversion technologies not only reduces the concentration of CO_2 in the environment, but also converts it into many useful chemicals like ethane (C_2H_6), methane (CH_4) and carbon monoxide (CO) [2]. This technique can be divided into four types: thermochemical conversion, biochemical conversion, photochemical conversion, and electrochemical conversion [3]. Among all the approaches, electrochemical conversion of CO_2 is one of the most promising strategies due to its mild operating conditions, utilization of renewable sources of energy and controllability of the process [3]. However, electrochemical CO_2 reduction reaction (CO_2RR) faces several difficulties. Firstly, CO_2 molecule has a stable structure which means the reduction of CO_2 needs to overcome high energy barrier to break the C-O bonds. Secondly, the electrochemical conversion involves multiple-electron transfer leading to a slow electron transfer kinetics and low exchange current density [4]. Also, competing hydrogen evolution reaction (HER, $2H^+ + 2e^- \rightarrow H_2$) in aqueous media, causes poor efficacy and stability. Therefore, it is urgent to develop effective electrochemical catalysts for CO_2RR.

In the past years, various materials have been studied and reported as catalysts for CO_2 reduction such as metals, metal oxides, transition metal dichalcogenides, conducting polymers and MOFs [5]. Among all these catalyst materials, MOFs have

attracted the attention of many researchers due to their unique advantages. MOFs belong to a class of porous and crystalline materials which are constructed by metal centers and organic ligands [5]. MOFs have high porosity, high electrochemical active , surface area as well as abundant catalytic sites and can be categorized under single atom catalysts [1]. Also, through rational design and synthesis, MOFs show tunable physical and chemical properties which can be engineered to different applications and performance. These advantages make MOFs one of the most promising candidates for catalytic CO_2 reduction. However, regarding their catalytic activity, MOFs also have some limitations such as low conductivity which needs to be further improved. In particular, dispersing metal ions on two-dimensional (2D) MOFs can further improve the conductivity and enhance electrocatalytic performance which make them very promising catalysts for CO_2RR [6]. Among these, Copper (Cu)-based MOFs show excellent catalytic activity as Cu-based materials can reduce CO_2 to highly reduced products such as CH_4 and ethane (C_2H_4) in room temperature [1].

1.2 Objectives

The thesis mainly focuses on the catalytic performances of Cu-based MOFs, especially 2D Cu-based MOFs towards CO_2RR. In this project, three MOFs are investigated: Cu-BTC (BTC = 1,3,5-benzenetricarboxylate, also known as $Cu_3(BTC)_2$ or HKUST-1), Cu-HAB (HAB= hexaaminobenzene, also known as $Cu_3(HAB)_2$) and Cu-HHTP (Cu_3(2,3,6,7,10,11-hexahydroxytriphenylene)$_2$ [$Cu_3(HHTP)_2$]), among which Cu-BTC is a conventional 3D MOF and other two are 2D MOFs. In particular, Cu-HAB has not been studied as CO_2RR catalyst before. In this thesis, the surface morphology, electrochemical performance of these three MOFs will be investigated. Furthermore, the product selectivity of Cu-HAB and Cu-HHTP will be researched and compared.

1.3 Approaches

To better investigate the potential of 2D Cu-based MOFs as CO_2 catalysts, characterization and electrochemical tests were developed, respectively. Scanning Electron Microscopy (SEM), Energy Dispersive Spectroscopy (EDS) and Fourier-transform infrared spectroscopy (FTIR) were used to understand the morphological features and bond structures of the sample. The electrochemical activity was examined using traditional electrochemical technologies in three-electrode system. And the products were tested using Gas Chromatography (GC) and Nuclear Magnetic Resonance (NMR).

1.4 Structure of the thesis

The thesis is mainly divided into 6 parts. The first part is a brief introduction to CO_2RR. And the second part introduces theorical knowledges which includes fundamental of CO_2RR and common electrochemical catalysts used. In the third chapter, catalytic performance indicators, the techniques used and the synthesizing process of Cu-HAB will be described. Then the experimental results of three MOFs and discussions are shown in the fourth part. Next, the final conclusion and future outlook are given in the fifth and last section, respectively.

2

Theorical study

2.1 Fundamentals of electrocatalytic CO_2RR

Half reaction of CO_2RR	Electrode potential E vs. SHE (V)
$CO_2(g) + H_2O(l) + 2e^- = HCOO^-(aq) + OH^-(aq)$	-0.43
$CO_2(g) + H_2O(l) + 2e^- = CO(g) + 2OH^-(aq)$ -	-0.52
$CO_2(g) + 3H_2O(l) + 2e^- = HCOH(l) + 4OH^-(aq)$	-0.89
$CO_2(g) + 5H_2O(l) + 6e^- = CH_3OH(l) + 6OH^-(aq)$	-0.81
$CO_2(g) + 6H_2O(l) + 8e^- = CH_4(g) + 8OH^-(aq)$	-0.25
$2CO_2(g) + 8H_2O(l) + 12e^- = C_2H_4(g) + 12OH^-(aq)$	-0.34
$2CO_2(g) + 9H_2O(l) + 12e^- = CH_3CH_2OH(l) + 12OH^-(aq)$	-0.33

Table 1. Common CO_2RR half-reactions and corresponding potentials in aqueous solution (1.0 atm, 25 °C, PH=7, and 1.0 M concentration of other solutes) [8].

The electrochemical reduction of CO_2 involves multi-electrons reduction reactions which can generate a large number of different intermediates and products. Table 1 shows part of the common CO_2RR half-reactions and corresponding potentials in aqueous solution at 1.0 atm, 25 °C and neutral PH.

However, the reduction of CO_2 faces many difficulties. CO_2RR usually happens in aqueous solutions. This means that it needs to compete with Hydrogen Evolution Reaction (HER) causing poor selectivity for carbonaceous products [2]. Additionally, the distance between C-O bond in CO_2 molecule (116.3 pm) is smaller than C-O single bond and many C-O bonds in other molecules such as the C–O bond in carbonyl (123pm) [1]. Therefore, CO_2 molecule is highly stable and static which results in higher energy demands to break its bonds to start the reaction. Moreover, low solubility of CO_2 in water (almost 0.034 M) is adversely affecting such diffusion-controlled reactions. The sluggish kinetics of CO2RR requires a larger negative potential to drive

the reaction than E^o values [1]. The formation of $CO_2^{\bullet-}$ radical anion intermediate requires a large negative potential -1.9V vs. hydrogen reference electrode (SHE) which further increases the difficulty of CO_2RR [1]. Considering all these challenges, the necessity of finding suitable electrocatalyst materials has received great attention by many research groups.

The process of electrochemical CO_2RR mainly involves three steps: Firstly, CO_2 will be chemical adsorbed on the surface of catalysts followed by a series of electron transfer. C-O bond is cleaved and related intermediates forms in this step. The last step is the rearrangement of intermediates to products which will desorb from the surface of catalysts to electrolyte [1]. The schematic illustration of CO_2 reduction is shown in figure 1. The electrochemical conversion of CO_2 is usually performed in a three-electrode system with aqueous electrolytes [2]. During CO_2RR, the reduction reaction of CO_2 and water happens in the cathode, while the anode undergoes oxidation reaction of water also known as oxygen evolution reaction (OER). As can be seen in the scheme, working electrode is used as cathode. And electrode in the middle is reference electrode, which usually uses SHE, silver chloride electrode (Ag/AgCl) and saturated calomel electrode (SCE). on the other side of the cell, anode is consisted of counter electrode (usually Platinum (Pt) electrodes are used) [2].

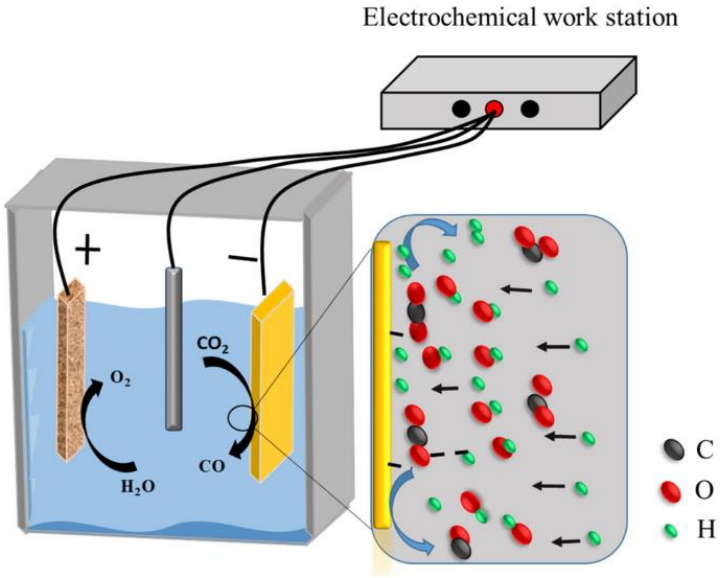

Figure 1: Schematic illustration of CO_2RR in a three-electrodes system [2].

Considering heterogeneous CO_2RR occurs at electrode-electrolyte interfaces, it's important to understand the interfacial region detailly. Figure 2 shows the interfacial regions of working electrode. During the electrocatalytic reduction of CO_2, the surface of cathode will be charged with electrons as a negative potential is applied. This leads to a strong interaction between cathode surface and molecule/ions in the solvent and forms a region called electrical double layer (EDL). EDL is consisted of oriented dipoles or charged species [1]. The interface can be divided into 5 regions [1].

- The surface of cathode;
- Inner Helmholtz plane (IHP);

- Outer Helmholtz plane (OHP);
- Diffuse layer;
- Bulk of the electrolyte.

IHP is the closest layer to cathode which mainly comprises reaction intermediates, products and absorbed reactants, etc. OHP is consisted of cations in the electrolyte which interact with cathode via electrostatic forces [1]. And diffuse layer is comprised with free ions that move in the electrolyte under the electrical forces and thermal motion [9]. During the CO_2RR, the adsorption and rearrangement of CO_2 molecules happen in IHP. When CO_2 molecules are absorbed to the surface of cathode, reactions happen with both electrode and electrolyte. Therefore, CO_2RR process is influenced by a series of factors such as concentration gradient, interactions of electrolyte ions with electrode surface and absorbed species and their influences on EDL, reaction activity and product selectivity[1].

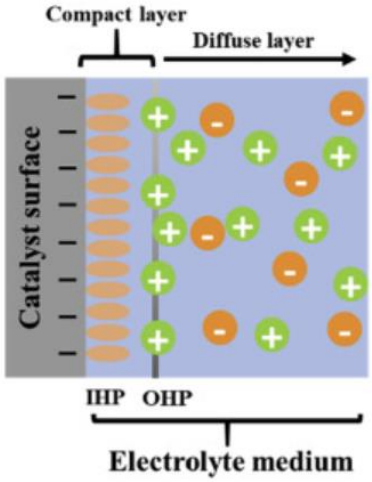

Figure 2: Schematic illustration of electrical double layer at cathode[1].

2.2 Performance indicators for electrocatalytic CO_2RR

To better analyze the performance of the catalysts, it's necessary to understand the performance indicators for CO_2RR. In this part, common catalytic performance indicators will be introduced.

2.2.1 Faraday efficiency

Considering CO_2RR needs to compete with HER, there is a large amount of input energy consumed by HER. To avoid undesirable waste of electricity and facilitate the separation of products, high selectivity is important [1]. The product selectivity is usually represented by faraday efficiency (FE) which can be calculated by Eq 2.4.

$$FE = \frac{nFN}{Q} * 100\% \qquad (2.4)$$

Here n is the number of electrons transferred per mole of product, F is the Faraday constant, N represents the number of moles of product obtained in electrolysis and Q is the total charge consumed during the electrocatalytic process [1].

2.2.2 Overpotential

Overpotential (η) is another important indicator which defines as the absolute value of the difference between the applied potential E and equilibrium potential of the relating half reaction E^{eq} [1]. It represents the extra voltage needed compared to thermodynamic prediction.
The equation is shown in Eq 2.5.

$$\eta = |E - E^{eq}| \qquad (2.5)$$

2.2.3 Current density

The current density can effectively show the reaction rate of the reaction. This is because the number of transferred electrons is proportional to the extent of reaction [10]. Higher current density means higher rate of reactant consumption. And a higher partial current density (FE*current density) towards specific product indicates a higher generation rate [10].

2.3 Common Electrocatalysts for CO_2RR

To achieve the effective electrochemical conversion of CO_2, catalysts are necessary. Four types of materials are widely studied as electrocatalysts for CO_2RR:

- Metallic catalysts and metal oxide;
- Carbon-based catalysts;
- State of the art 2D transition metal chalcogenides (TMDs);
- MOFs

2.3.1 Metallic Catalysts

The study of metallic catalysts for CO_2 reduction can date back to 1980s [11]. When metallic catalysts are chosen as catalysts, the first step of CO_2RR is to generate $CO_2^{\bullet-}$. Then after a series of electron and photon transfer, final products will be produced. To get good catalytic performance, the stabilization of intermediate on catalysts is very crucial. Metallic catalysts can be generally divided into 4 groups. The first group which includes Lead (Pb), Tin (Sn), Mercury (Hg), Indium (In) and Bismuth (Bi). This type of metal hardly absorbs $CO_2^{\bullet-}$ but prefers to bind with *OCHO intermediate and produce formic acid or formate as products [11]. And second group is the opposite. Metals such as Zinc (Zn), Sliver (Ag), Palladium (Pd) and Gold (Au) will bind $CO_2^{\bullet-}$ and then bind *COOH intermediate tightly which can eliminate water to form *CO. However, CO will be released as final product due to the weak binding between metals and *CO intermediate [12]. Cu is singularly categorized into a group because of its unique catalytic properties. Different from the metals in group 2, Cu can bind *CO very tightly due to its strong binding energy [12]. Therefore, *CO can be further reduced into many other valuable products such as CH_4 and C_2H_4. The metals in last group such as Pt, Titanium (Ti) and Iron (Fe) prefer to bind hydrogen and form H_2 as the main

product through HER reaction. The mechanism of metallic catalysts in CO_2RR is shown in figure 3. During the CO_2RR, the binding energy of the catalysts, roughness and size will largely influence the selectivity and activity.

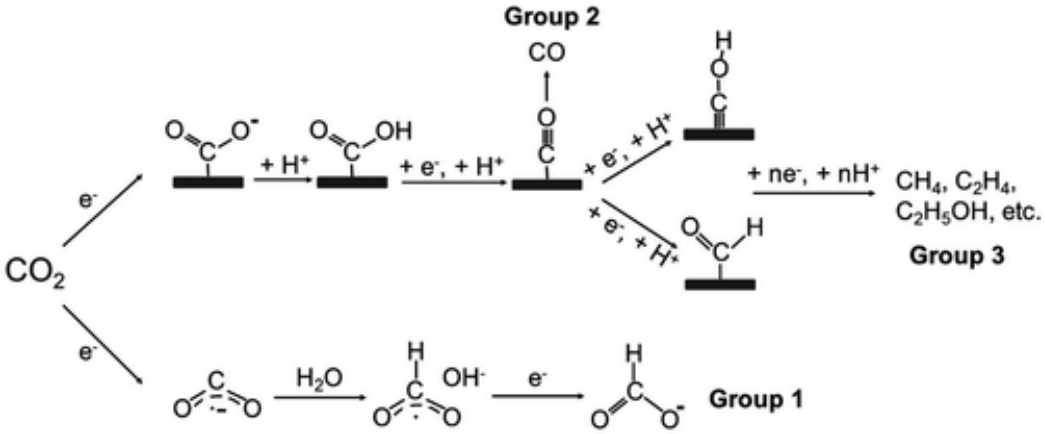

Figure 3: Schematic diagram of the mechanism of CO_2RR on metal surfaces [12].

However, though metallic catalysts show high FE for CO_2RR and high electron mobility. The low long-term stability and high price hamper their industrial utilization. Thus, transition metal dioxides (TMOs) are developed to improve long-term stability and increase charge transfer capabilities by increasing surface roughness and providing subsurface oxygen species [13]. For example, the O vacancies in Cu_2O crystals are be proved to be the active sites for C_2H_4 formation, indicating that TMOs can be useful for improving selectivity towards C_2 product. In this study, Cu_2O-derived Cu catalysts showed optimized FEs for C_2H_4 (42.6%), C_2H_5OH (11.8%) and total CO_2 reduction (70.1%) [14].

2.3.2 Carbon-based Catalysts

Compared to metallic material, carbon-based materials have unique advantages such as large surface area, abundant resource and better conductivity. In particular, graphene has received a lot of attention due to its 2D structure [15]. Although carbon-based materials are widely studied in HER process, they are rarely used for catalysts. The main reason is that graphene and graphene-like materials have low catalytic activities. This is because they can hardly adsorb and activate CO_2 due to their sp^2-conjugated structure composed of neutral carbon atoms [1]. By doping with heteroatoms such as N, B and S, the electronic properties and catalytic activities can be improved to some extent. Studies have shown that various carbon-based materials show capable activity with metallic materials after doping with heteroatoms [11]. For instance, nitrogen-doped carbon nanotubes (NCNTs) have been reported to reduce CO_2 to CO at low overpotential (-0.18V) and reach high product selectivity (80% FE), while pristine CNTs show poor catalytic activity and low selectivity (FE less than 20%) [16].

2.3.3 State of the art 2D transition metal dichalcogenides

The third type of commonly used catalysts is TMDs. TMDs are usually presented as MX_2 where M is a transition metal such as Molybdenum (Mo), Tungsten (W) and Nickel (Ni) and X represents a chalcogen such as Selenium (Se) and Sulfur (S) [17]. The structure of TMDs is constructed by three layers formed by X-M-X. The chalcogen atoms in two hexagonal planes are separated by a plane of metal atoms [17]. Two typical combination models for MX_2: trigonal prismatic and octahedral phase are shown in figure 4 (b-d). TMDs such as WS_2 and MoS_2 are widely studied as HER catalysts [18]. However, recently they are also considered as potential catalysts for CO_2RR. In stable TMDs, the pure basal planes are normally considered as inert. The edges and vacancies can serve as active sites for catalytic reaction (figure 4 e). The CO_2RR process using TMDs as catalysts should be carried out in ionic liquid solution to form a stable intermediate $CO_2^{\bullet-}$ and suppress HER [11]. The $CO_2^{\bullet-}$ intermediate can be stabilized on either metal or covalent sites and transferred to other products. Moreover, the 2D layer structure brings higher surface area for TMDs which can increase the active sites and increase catalytic activity [17]. The product of TMDs show high selectivity towards CO. According to the study by Asadi et al, MoS_2 shows 98% FE of CO at - 0.764 V versus the reversible hydrogen electrode (RHE) [19].
In general, TMDs are considered potential materials for CO_2RR. However, there are a lot of developmental problems of TMDs which mainly focus on how to maximize the active edges and improve the conductivity. Also, it's necessary to improve the stability of TMDs for CO_2RR and make the synthesis adapt large-scale industrial production.

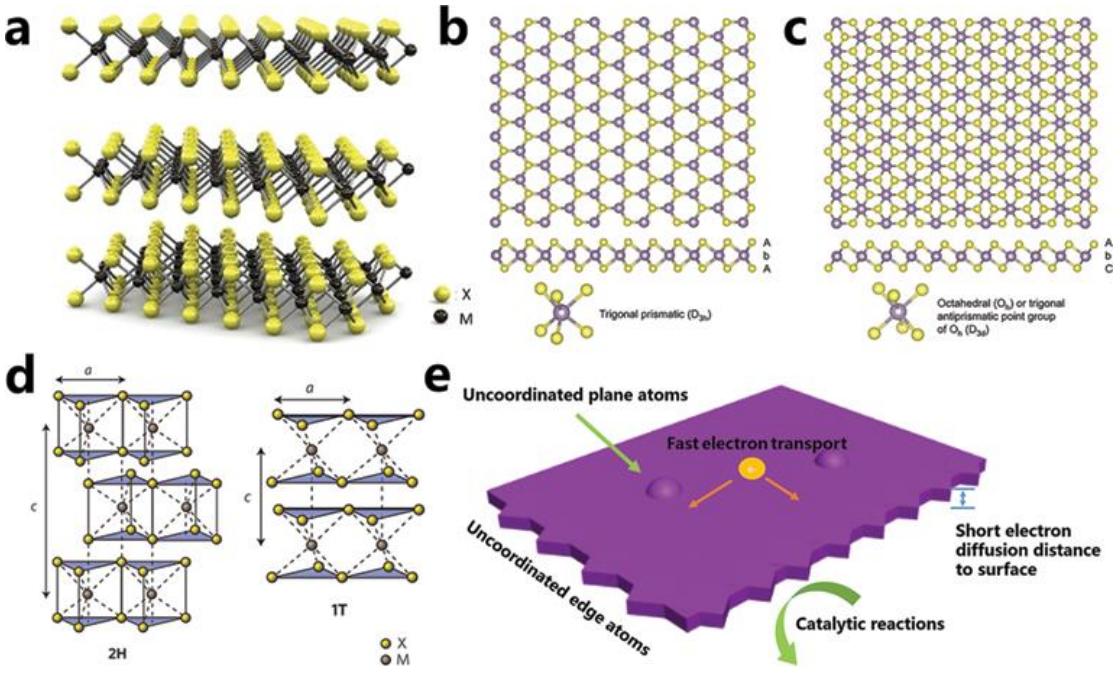

Figure 4: a) basic structure of TMDs. b) trigonal prismatic and c) octahedral coordination of TMDs from axis view and d) side view. e) schematic illustration of TMDs catalytic reaction [17].

2.3.4 Metal-organic framework

In the context of aqueous electrocatalytic CO_2 reduction, MOFs combine the favorable characteristics of both heterogeneous and homogeneous catalysts. Exploration of MOFs for CO_2 reduction has begun from their usage as photocatalysts in colloidal dispersions, however, with the aid of sacrificial reagents MOFs have only recently been utilized as electrocatalysts for CO_2 reduction [1]. MOFs are porous crystalline materials constructed from metal nodes and organic ligands. Compared to other materials, MOFs have hold great potential for CO_2RR due to their enormous surface area (extending beyond 6 000 m^2/g), ultra-high porosity (up to 90% free volume) and tunable structure [20]. Moreover, owing to the metal-ligand periodic interval of MOFs, active sites are in a state of monoatomic dispersion, which further promotes ECR. Single atom catalysts such as MOFs integrate the advantages of both homogeneous and heterogeneous catalysts.

MOFs have been studied and used in a series of electrocatalytic process such as HER, ORR and CO_2RR [11]. In the context of CO_2 reduction, they show high product selectivity towards different products such as CO, CH_4 and C_2H_4 depending on the MOF structure [11]. The first application of MOFs-related material as catalysts for CO_2RR started in 2012 [21]. At that time, Hinogami et al. used a copper rubeanate metal-organic framework (CR-MOF) as electrocatalysts to reduce CO_2 to HCOOH (FE≈100%) [21]. They were able to prove that compared to Cu, CR-MOF has higher selectivity and current density [21]. Although MOFs show encouraging results as electrocatalysts, there are also some limitations such as poor electrical conductivity and structural stability [22].

This problem can be alleviated by dispersing metal ions on 2D MOFs which can further improve the conductivity and enhance electrocatalytic performance which make them very promising catalysts for CO_2RR [23]. 2D MOFs are constructed of metallic sites and conjugated organic linkers with multitopic ortho-substituted functional groups such as -NH_2 and -OH [23]. Some typical organic linkers and relevant 2D MOFs are shown in figure 5. The structure of 2D MOFs is feasibly tailored by ligand design which results in different pore geometries such as hexagonal square and triangle shape. Also, the size of pore can also be adjusted from non-porous to 2nm in diameter [23]. Now, there have been various methods to synthesize 2D MOFs which include solvothermal method, surfactant-assisted method and interface-assisted method, etc [23]. Due to the strong in-plane conjugations and compact out-of-plane π-π stacking, the 2D lattices of MOFs are periodically arranged to form later-stacked framework with high porosities, electrical conductivity and abundant catalytic active sites [23].

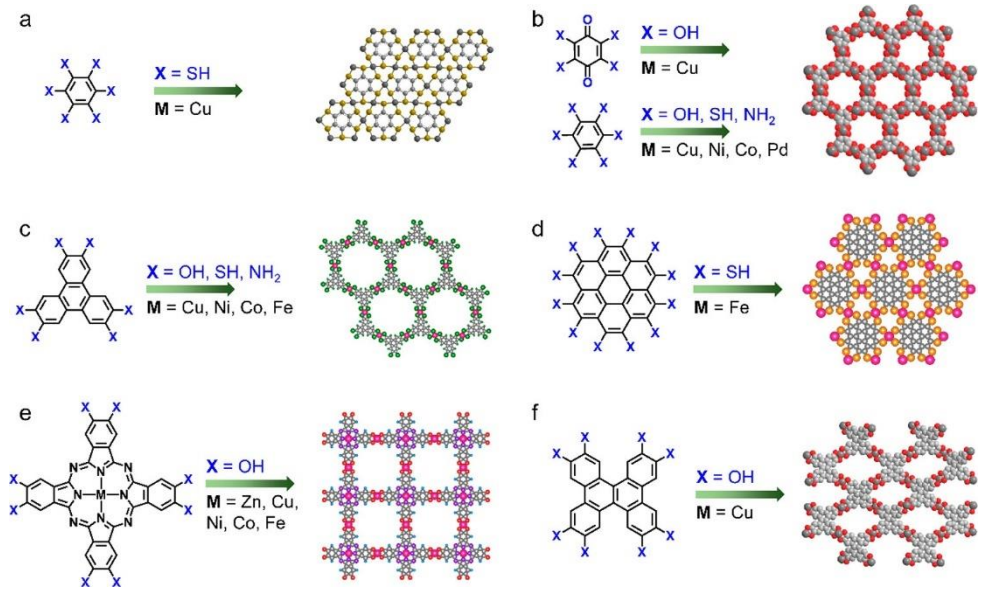

Figure 5: Typical organic ligands and the relevant 2D c-MOFs. (a) Benzene-based, (b) benzoquinone/benzene-based, (c) triphenylene-based, (d) coronene-based, (e) phthalocyanine-based, and (f) dibenzo[g,p]chrysene-based ligand monomers [23].

For instance, a 2D Cu-based c-MOF, copper tetrahydroxyquinone (Cu-THQ) nanoflakes shows little overpotential (16mV) to activate the reaction, high current density (≈173 mA cm^{-2} at −0.45 V versus RHE) and high FE (≈91%) towards CO (are shown in figure 6) [24].

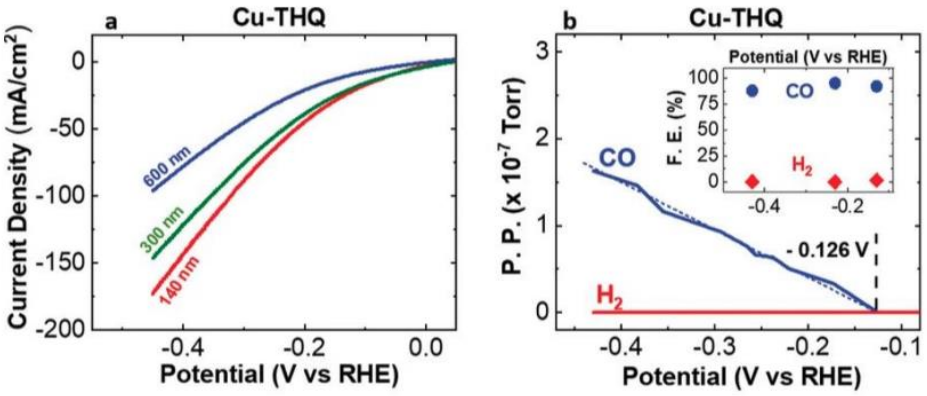

Figure 6: a) LSV results of Cu-THQ NFs of different particle sizes for electrochemical CO_2 reduction in 1 m choline chloride and 1 m KOH at 50 mV/s. b) DEMS results of Cu-THQ NFs for CO and H_2 production during LSV experiment with scan rate of 1 mV/s [24].

In general, 2D MOFs are considered as one the most promising catalysts for CO_2RR. To better express the advantages of 2D MOFs, both selection of metal sites and ligand engineering are crucial [23].

2.4 Cu-based MOFs for CO_2RR

Among all the MOFs, Cu-based MOFs draw much attention because they can be synthesized with commercially available materials and have especially large surface area [25]. And Cu is considered as one of the most attracting metal materials for MOFs due to its low cost, abundance of resource and high complexation strength [25]. Moreover, Cu can produce different hydrocarbons at high rate which make it attracting candidate for CO_2RR. In this part, three kinds of Cu-based MOFs will be introduced: Cu-BTC, Cu-HAB and Cu-HHTP.

2.4.1 Cu-BTC MOF

Cu-BTC is one the most widely studied MOFs due to its large surface area, high stability, highly porous structure and ability to bind with other molecules with its unsaturated Cu (II) site [26]. The synthesis of Cu-BTC first proposed in 1999 by Stephen Chui and co-workers [27]. Cu-BTC is comprised of large central cavity surrounded with small octahedral cages [28]. In the structure of Cu-BTC, two Cu metal atoms are bonded with 4 oxygen atoms from BTC linkers to form four connected square-planar vertexes and another axial coordination sites are regarded as open metal sites [29]. The three-dimensional (3D) structure of Cu-BTC is shown in figure 7.

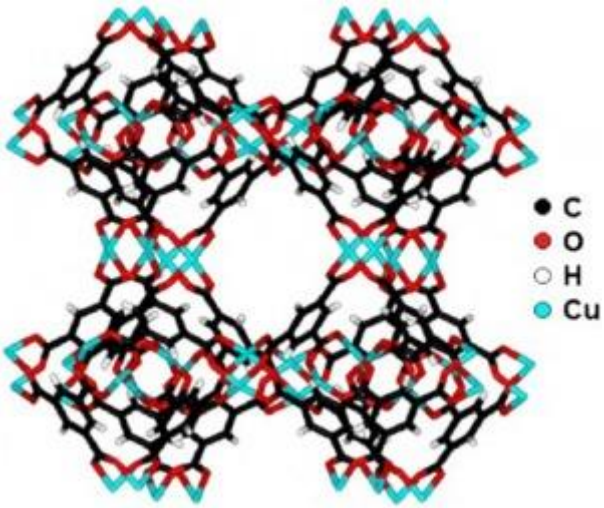

Figure 7: The chemical structure of Cu-BTC [30].

The open metal Cu (II) sites act as active sites for CO_2 adsorption and catalysis [31]. Moreover, the high CO_2 adsorption capacity makes it a strong candidate as catalysts for CO_2RR [30]. There have already been some reports on Cu-BTC catalysts for CO_2 reduction. For example, Kumar et al. reported a successful case which reduce CO_2 on Cu-BTC films into oxalic acid (FE=51%) [26]. And there are also many studies which focus on improvements to catalytic performance of Cu-BTC by making composites or changing the size of crystals.

2.4.2 Cu-HAB MOF

Different from Cu-BTC, Cu-HAB has a 2D structure. 2D MOFs play important role in electrocatalysis. The metal nodes and organic ligands can serve as the source of charge carriers and improve the whole electrocatalytic ability [32]. In addition, HAB molecule is highly conjugated and delocalized which can coordinate with metal cations very well [32]. Also, HAB is one of the smallest linkers which can perform significant 2D chelating effect to enhance the thermal and kinetic stability [33]. Figure 8 shows the structure of Cu-HAB. Cu ions are connected with HAB linkers to form 2D periodic lattice. Each Cu ion connects with 4 N atoms in a square-planar symmetry which forms subnanometre pores [33]. This kind of structure leads to dense framework and high volumetric capacitance. Dawei et al have reported that Cu-HAB shows good chemical stability in aqueous solutions and has high volumetric capacitances [33]. These properties make it a very potential material in the application of energy storage and conversion. It's expected to have a good performance as catalysts for CO_2 reduction.

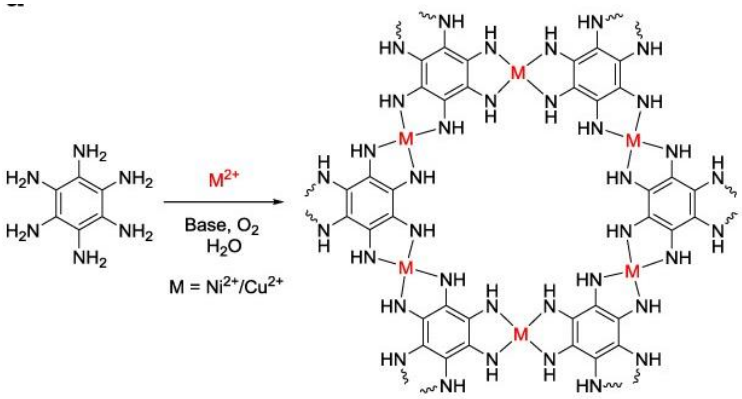

Figure 8: Structure of Cu-HAB, M represents metal atoms (Cu) [33].

2.4.3 Cu-HHTP MOF

Cu-HHTP is a kind of 2D semiconductive framework which has been widely investigated for the application of Li-ion battery and sensors [34]. It's first synthesized by Yaghi et al by linking Cu^{2+} ions with highly conjugated linker HHTP [35]. The structure of Cu-HHTP is shown in figure 9. The building units of Cu-HHTP is consisted of Cu^{2+} ions coordinated with HHTP redox-active ligands and form 2D extended sheets [33]. The Cu-O_4 nodes are periodically arranged in the honeycomb-like porous structure which are beneficial for electrochemical conversion of CO_2 [36]. According to the study by Yu Zhang et al, the FE of Cu-HHTP during ECR test is over 65% which indicates inhibited HER process [36]. This means Cu-HHTP is also a very potential catalytic material for CO_2 reduction.

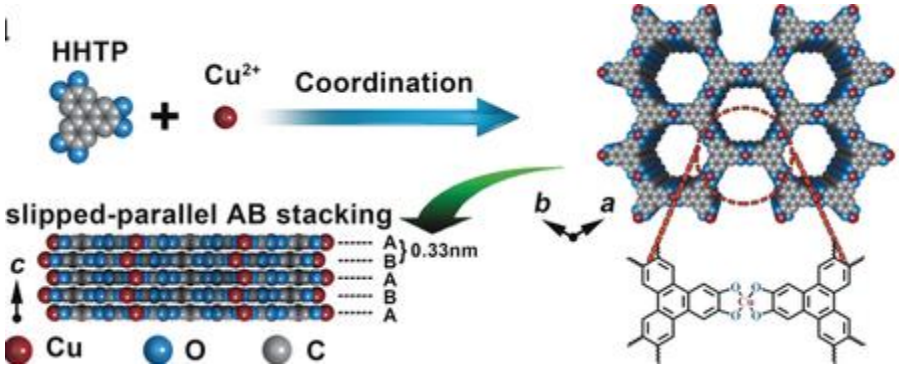

Figure 9: The crystal structure of Cu-HHTP [37].

3

Experimental section

This section mainly introduces the materials and methods used during experimental work. In this project, Cu-BTC and Cu-HHTP were commercially bought from Sigma Aldrich and CD Bioparticles respectively and used without any modification, while Cu-HAB was synthesized. In this part, the brief synthesizing method of Cu-BTC and Cu-HHTP, specific synthesizing process of Cu-HAB, the ink formula for working electrode samples and the technique used for characterization and electrochemical measurements will be discussed detailly.

3.1 Synthesis of Cu-BTC and Cu-HHTP

In this project, Cu-BTC and Cu-HHTP were commercially bought from Sigma Aldrich and CD Bioparticles. And this part will introduce the typical synthesizing methods of the two materials briefly. First, the typical synthesis of Cu-BTC uses Cu $(NO_3)_2 \cdot 3H_2O$ dissolved in deionized water and H3BTC dissolved in EtOH. The two solutions are mixed together with specific amount of water in an autoclave. Then the autoclave is heated at 120 °C for 12 h before being cooled to ambient temperature to get the final product [38].

And the synthesis of Cu-HHTP uses a solid mixture of HHTP and $Cu(C_5H_4F_3O_2)_2$ dissolved in deionized water. Then NMP (n-methyl-2-pyrrolidone) is added dropwise. Next, heat the reaction mixture in an isothermal oven at 85 °C for 12 h, wash the resulting crystals with deionized water, and then acetone and dried in air to get the final product [36].

3.2 Synthesis of Cu-HAB

During the synthesizing process, copper nitrate hemi(pentahydrate) (Cu $(NO_3)_2$ ▪$5H_2O$) was used as the copper precursor and Hexaaminobenzene trihydrochloride (HAB▪3HCL) as HAB precursor. First, 35mg Cu $(NO_3)_2$ ▪$5H_2O$ was diluted in 5ml water. Then add the solution and 0.4ml of concentrated aqueous Ammonium hydroxide

(NH_4OH) to a solution of 15mg of HAB▪3HCL in 5ml water. Next, the mixture was stirred for 10 minutes and left to rest for 2 hours at room temperature as the crystal growth. The resulting black powder was centrifuged, washed with isopropanol (IPA) and centrifuged again. Finally, the solid was dried in the oven at 60 degrees [33]. Figure 10 shows the schematic diagram of synthesizing process.

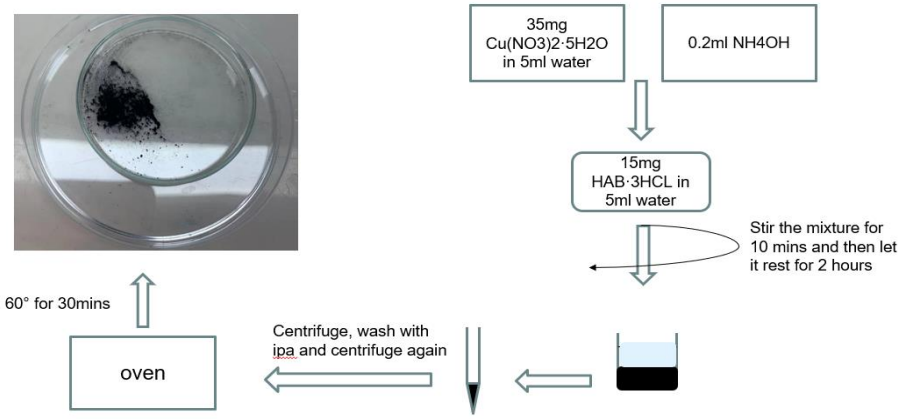

Figure 10: A schematic diagram of the synthesizing process for Cu-HAB.

3.3 Preparation of working electrode

Before starting electrochemical measurements and product analysis, working electrode need to be prepared out of MOF powders. The working electrode was prepared by drop-casting the ink on top of clean glassy carbon substrate. The glassy carbon is electrochemically inert under a large range of potential which makes it an ideal substrate for electrochemical measurements. Carbon paper and carbon cloths can also be used as substrate. Compared to glassy carbon, carbon paper and carbon cloths can better control the surface area and the amount of ink, while glassy carbon is harder and easier to prepare and do the whole test [39]. The specific preparation steps of working electrode are shown below.

Clean the substrates

Glassy carbon substrates were cleaned with deionized (DI) water and a cloth. Then they were placed in a test tube with some DI water in and sonicated for 10 minutes. The same procedure was repeated with IPA. After sonication, the substrates were dried with a flow of compressed air.

Ink preparation

After cleaning the substrates, the next step is to prepare the ink. The main components of ink are active material (AM), binder and conductivity enhancer. In this project, Polyvinyl alcohol (PVA) was used as binder and carbon black (CB) as conductivity enhancer. The weight ratio of AM, PVA and CB is 18:1:1e.

The ink preparation steps are as follow:

First, about 60 ul 5 wt% PVA was added to a vial and record the weight. Then the amount of CB and MOFs were calculated accordingly and were added into the vial.

Next, 2ml of DI water was added to the slurry, the vial was sealed and the ink was sonicated for about 30 minutes. The ink is ready to be drop-casted.

Drop-cast the ink

Approximately 20 uL of ink was drop casted with the micropipette on a cleaned glassy carbon substrate and it was spread evenly.

Let the ink dry

The ink was left for several hours until completely dry.

3.4 Characterization techniques

To better understand the surface morphology and structure of the sample, characterization is necessary. Here, SEM, EDS and FTIR were used to characterize the MOFs.

3.4.1 SEM

SEM is an important microscopy technique which can be used to detect the surface morphology of the sample. During the measurement, the sample is shotted by electrons with high energy [40]. When electrons hit the surface of the sample, the secondary and backscattered electrons will be generated and detected by the detector [40]. These outcoming signals give the information of elemental composite, surface morphology and crystalline structure [40]. Compared to traditional light microscopes, SEM has shorter wavelength which enables much better resolution. Though SEM cannot provide internal information of the sample, it can give variable information about size, texture and surface features [40]. In this project, SEM is used to analyze the surface morphology of the sample. The SEM (JSM-IT100) equipped with a JEOL-made EDS was used to study the morphology of tested samples in this work. The working voltage is set as 10kV and working distance is 10mm.

3.4.2 EDS

EDS technique is usually used for qualitative or semi-quantitative analysis of the material. The EDS system is equipped in the SEM instrumentation. It can be used to characterize the elemental composite by analyzing the X-rays emitted after bombardment by the electron beam [41]. When the sample surface is bombarded by electron beam, electrons will be ejected from the atom and electrons from higher state will fill in the resulting vacancies [41]. Then X-ray is emitted to balance the energy difference. The energy of X-ray is determined by the elements of the atom which allows elemental characterization [41]. The EDS measurements were performed using same working voltage with SEM measurements.

3.4.3 FTIR

Except surface morphology and elemental characterization, bond analyzation is also important to better understand the structure and properties of the material. Bond structure can be characterized by FTIR. FTIR is a technique which can obtain an infrared spectrum of absorption or emission of a solid, liquid or gas [42]. The detection is related with the vibration of molecules. Different functional groups have their own

different vibrational energy which can be used to identify molecules [43]. The main components of FTIR are the source, interferometer, and detector. The schematic diagram of FTIR is shown in figure 11.

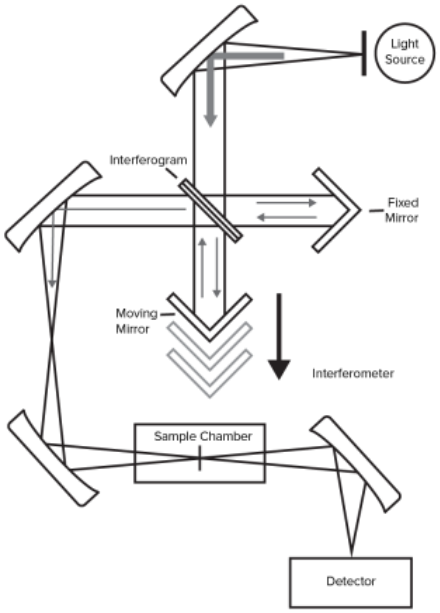

Figure 11: Schematic diagram of FTIR [43].

The source commonly uses a broadband emitter such as a far-IR mercury lamp, a near-IR halogen lamp and a mid-IR ceramic source [43]. The infrared energy is emitted from the source and passes through an aperture which controls the energy presented on the sample [44]. Interferometer is the core component of FTIR which consists of a beam splitter, a stationary mirror, a moving mirror, and a timing laser [43]. The beam splitter splits the light into two paths which 50% is refracted to the fixed mirror and 50% will transmit through the moving mirror [43]. Later the separated beam will be recombined back to the beam splitter and stirred to the sample [43]. The constructive and destructive interference will happen due to the difference in the paths of two mirrors [42]. Then the interferogram can be obtained by recording the signals versus different mirror position [42]. The high speed and sensitivity make FTIR ideal technique for sample identification, particle analysis and film characterization in various applications [43].

In addition, because a relative scale is needed to detect the absorption intensity, a background must be measured first [44]. The background normally uses same substrate without sample (glass is used in this project).

3.5 Electrochemical measurements

To better measure the catalytic activities of samples, a series of electrochemical measurements were performed. In this part, the electrochemical techniques used and corresponding working principles will be discussed.

3.5.1 Cyclic Voltammetry

Cyclic Voltammetry (CV) is an important electrochemical measurement which can be used to test the redox properties of the material. CV is usually performed in a three-electrode system which consists of working electrode, reference electrode and counter electrode. Here, the working electrode is prepared using glassy carbon drop-casted with ink. The reference electrode used is SCE and Pt net is used as counter electrode. The experimental setup is shown in figure 12.

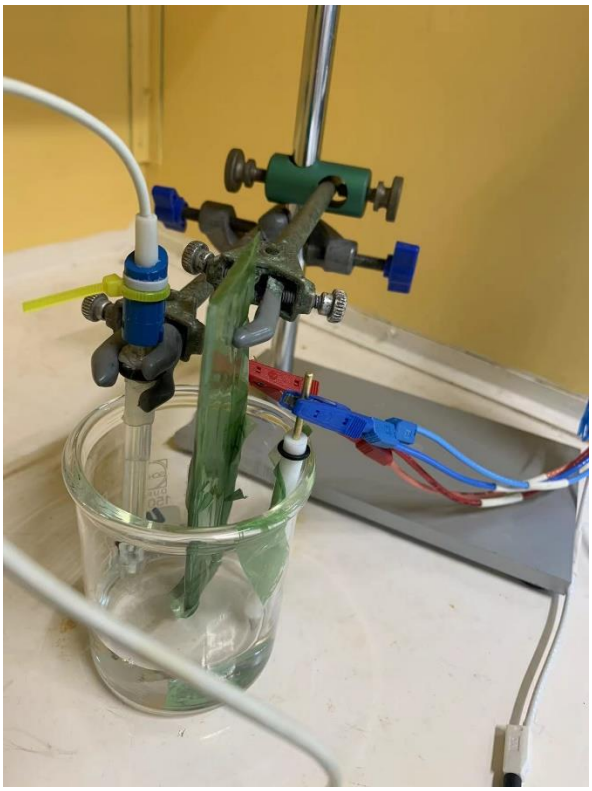

Figure 12: Experimental setup for electrochemical measurements.

During the measurement, a potentiostat is used to linearly sweep the potential between the working and reference electrodes. After the potential reaches the set value, the potential applied will go in the opposite direction and return to the initial value [45]. A VSP-300 (Biologic) potentiostat was used to perform electrochemical experiments. In this project, CV measurements were conducted in 1 M $KHCO_3$, with scan rate of 100 mV/sec in a potential range of -0.5 to 0V vs. SCE.

3.5.2 Linear Sweep Voltammetry

Linear sweep voltammetry (LSV) is another basic electrochemical voltametric method which measures the current passing through the working electrode while the potential swept linearly in time. LSV uses the same three-electrode system as CV measurement. However, different from CV, LSV sweeps the potential in one direction which is equivalent to a one-segment CV curve [46]. During the measurement, the potential is linearly swept from initial value to final value, and the current is sampled at specific intervals. LSV can provide quantitative and qualitative information of electrochemical reactions and is considered as a very reliable characterization tool for CO_2RR. When a reduction reaction happens at the surface of working electrode, the molecules on the surface are reduced or oxidized and then flow away from the surface. The motion of electrons will lead to the change in current. The current measured depends on the rate of exchanging electrons through working electrode interface. When the rate gets higher enough for oxidizing or reducing species to diffuse from the electrolyte to the surface of electrode, then current reaches a peak or plateau [47]. During this project, all LSV experiments were performed using a VSP-300 (Biologic) potentiostat in the same electrolyte as CV measurements with the scan rate of 50mV/s in a potential range of -2 to 0.1V vs. SCE.

3.5.3 Electrochemical Impedance Spectroscopy

Next, electrochemical Impedance Spectroscopy (EIS) is a power electrochemical technique which gained a lot attention in the past 10 years [48]. One of the most important reasons is that EIS allows separating measurements of different components such as double layer capacitance and electron transfer resistance [48]. Also, the surface sensitivity of EIS is very high. This means it can detect many small changes over the surface that other techniques may not see. During electrochemical measurements, EIS can relate the actual electrochemical processes with relating theoretical circuit elements. A typical electrochemical process contains several basic components such as electric double layer and faraday reaction. Schemes of redox reaction on the surface and equivalent circuit are shown in figure 13.

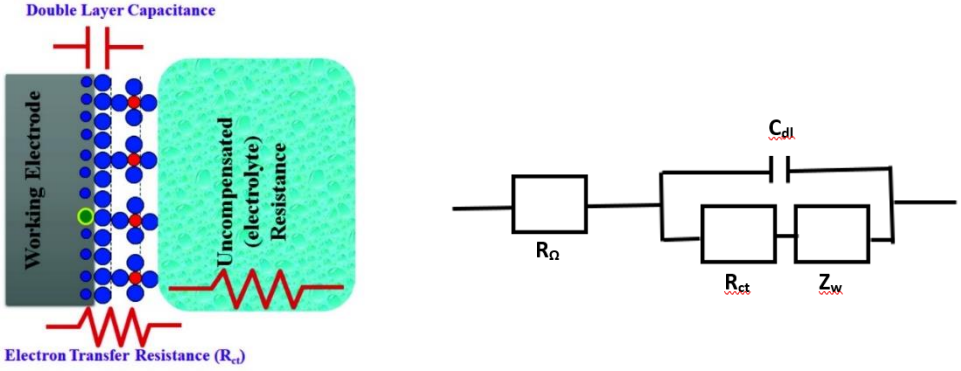

Figure 13: Schemes of redox reaction on the surface and equivalent circuit [49].

Correspondingly, the total impedance of the process can be abstracted into three electrical components: the charge transfer resistance R_{ct}, solution resistance R_{Ω} and the double layer capacitance C_{dl}. In addition, diffusion can cause extra impendence Warburg impedance Z_w. The impendence depends on the frequency of the potential perturbation [49]. When the frequency is large enough, the Warburg impedance will become very small because there is not enough time for mass transformation [49].

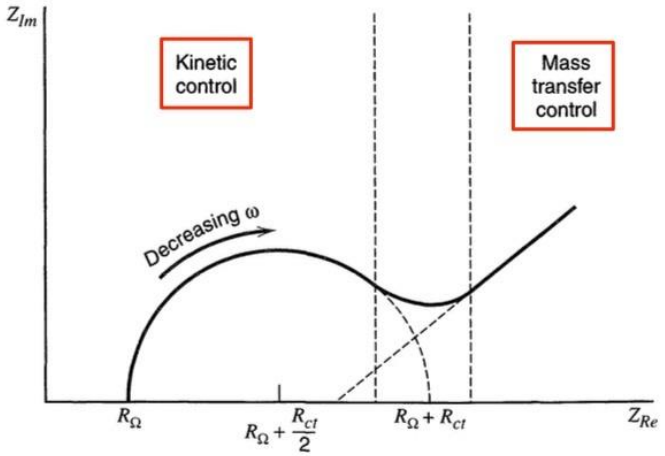

Figure 14: “Nyquist Plot" according to the equivalent circuit [50].

By plotting the real part and imaginary part of the whole impedance, a “Nyquist Plot" can be obtained (figure 14). The low-frequency region is under kinetic control, while high-frequency region is controlled by mass transfer [50]. In the case of the effect of Warburg impedance disappears, the “Nyquist Plot" shows a full semicircle. The diameter of the semicircle represents the charge transfer resistance which decides catalytic kinetics during the electrochemical reaction process. During the project, all EIS experiments were performed using a VSP-300 (Biologic) potentiostat in the frequency range of 100mHz to 1MHz in 1M $KHCO_3$.

3.5.4 Chronoamperometry

Addition to other electrochemical measurements, to better understand the catalytic stability of the samples, Chronoamperometry (CA) was performed to record the variation of current with time under constant potential. It’s widely used in electrochemistry because of the easy analyzing process and high sensitivity. In this thesis, CA measurements were conducted together with gas chromatography (GC) under constant potential of -1.6V vs. Ag/AgCl for 60 minutes in 1 M $KHCO_3$.

3.6 Product analysis

Along with surface characterization and electrochemical measurements of MOFs, GC and NMR were used to detect the gaseous and liquid products of CO_2RR quantitatively to calculate the FE.

3.6.1 Gas Chromatography

GC is a powerful technique used to separate different gaseous chemicals of a mixture and detect each component quantitatively. The schematic of GC system is shown in figure 15. There are three main components in GC system: sample injector, column a detector. During the measurement, the gaseous sample will be injected into GC and flow through column by carrier gas. In the case of liquid sample, the sample injector will heat the sample and vaporize it into gaseous state which can flow into the column. The column is a long metal or fused silica tube coating with the stationary state on the walls. After the sample reaches column, different components in the sample will flow at own rate according to the different interactions with stationary states [51]. As a result, different components will be separated. Then the detector can analyze the amount of each component and convert it into electrical signal.

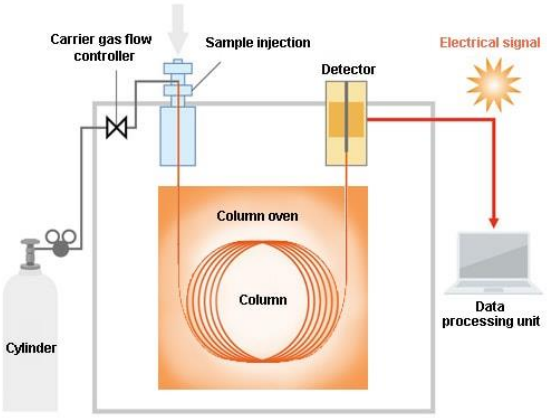

Figure 15: Simple schematic of GC system [51].

The GC device used in this project is CompactGC4.0 (GAS) which comprises of three columns to separate and detect different gaseous products. The first column connects to a flame ionization detector (FID) which can detect different products according to their different boiling point and vapor pressure. Considering FID is highly sensitive to hydrocarbons, column 1 is typically used to detect hydrocarbon products. And the other two columns are connected with thermal conductivity detectors (TCDs) which rely on different thermal conductivities between carrier gas and sample. Considering most compounds have much lower thermal conductivity than helium or hydrogen, when the sample elutes from the column, the thermal conductivity of effluent will reduce and produce detectable signal [52]. The second column uses helium as carrier gas to measure CO_2 and O_2, while the third uses Argon to detect hydrogen component. The electrochemical flow cell used for GC measurement is shown in figure 16. It contains cathodic and anodic chambers separated by an anion-exchange membrane from fumatech company. During the measurement, CO_2 gas was purged into the electrolyte in the cathodic side and react with working electrode, then the mixture of gaseous products was carried with CO_2 flow into the GC to be detected. In this study, all GC measurements were performed along with running CA analysis in 1.5 ml of 1 M $KHCO_3$ as electrolyte at -1.6 V vs.

Ag/AgCl. CO_2 flowing rate into the cell was set as 10 ml/min and the outlet gas was analyzed every 3 min.

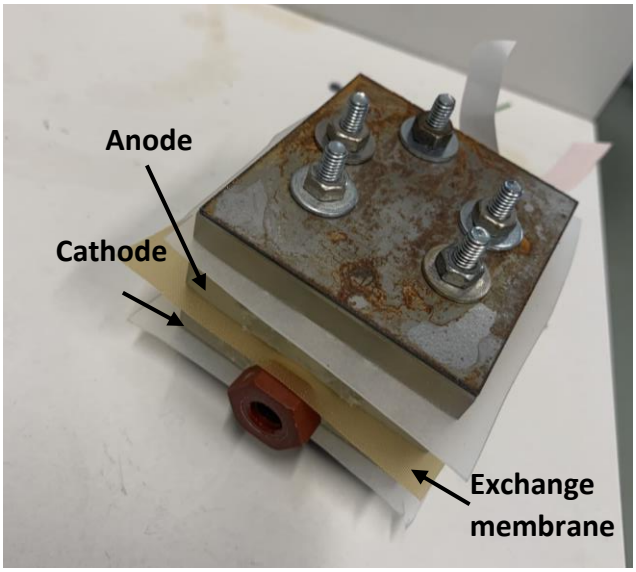

Figure 16: Electrochemical flow cell of GC measurements.

3.6.2 Nuclear Magnetic Resonance

And NMR is a kind technique which can observe local magnetic fields around atomic nuclei. Over the past years, it has become a powerful tool to determine the structure of compounds. The principle of NMR is based on the facts that many nuclei have spin and all nuclei are electrically charged. An overview of NMR is shown in figure 17. By applying an external magnetic field, energy transfer will happen from base energy level to higher energy level which corresponds to specific frequency. When the spin comes back to base level, the energy will be emitted at same frequency. Next, the signals are measured and processed to produce an NMR spectrum for nucleus concerned [53]. In this project, NMR tubes were cleaned with Acetone. And the NMR sample prepared used 0.63 ml of electrolyte mixed with 0.07 ml deuterium oxide (D2O, heavy water) and 0.03 ml phenol and Dimethyl sulfoxide (DMSO) solution.

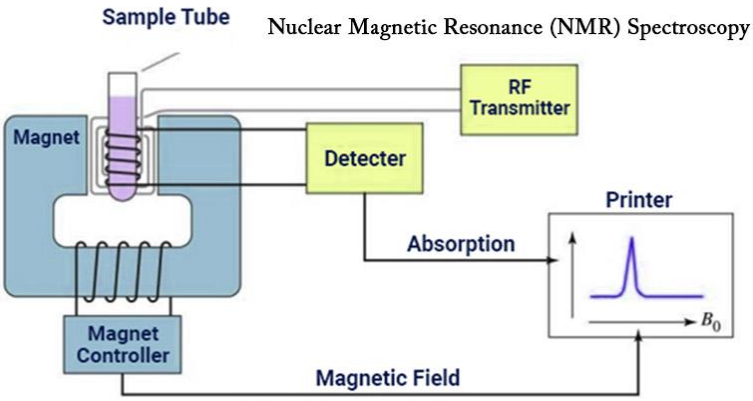

Figure 17: Schematic presentation of a typical NMR [53].

4

Results and Discussion

In this section, the experimental results for surface characterization, electrochemical measurements and product analysis of Cu-BTC, Cu-HAB and Cu-HHTP will be presented and discussed.

4.1 Surface characterization

4.1.1 SEM and EDS

Cu-BTC

To better understand the structure and elemental composition of Cu-BTC sample, SEM and EDS were performed under 10 kV working potential. The sample prepared by dropping-cast Cu-BTC ink in IPA on top of the glassy carbon substrate. The SEM graphs show clear cubo-octagonal shaped crystals of Cu-BTC which are identical to the previous reports [54]. As can be seen in figure 18a-c The size of crystals is in the range of 20-40 µm without any aggregation. Besides, there are some crystals in pyramidal shape which are supposed to be metal oxide by-products CuO_x [55].

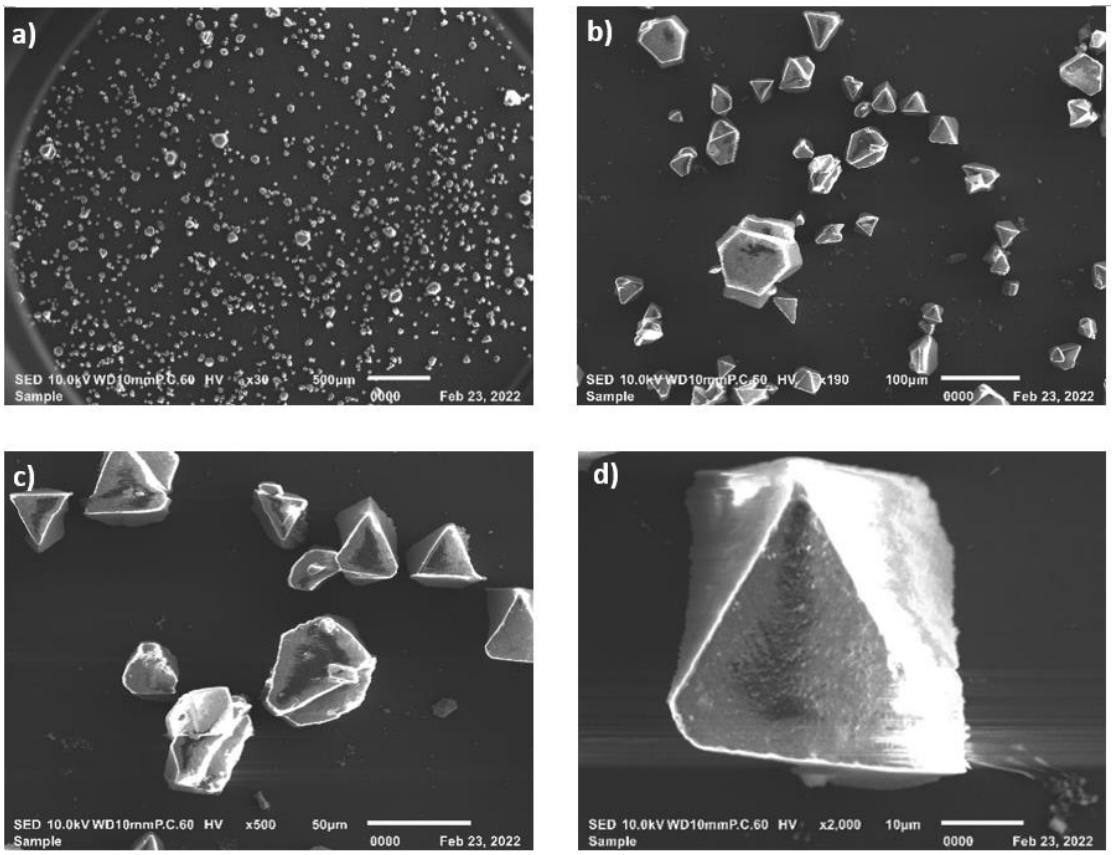

Figure 18: SEM images of Cu-BTC sample. The scale bar corresponds to (a) 500 µm, (b) 100 µm, (c) 50 µm, (d) 10 µm.

Then EDS was used to better understand the elemental composition of Cu-BTC sample. Figure 19 shows the element peaks of Cu-BTC sample and table 2 further presents the mass percentage and atom percentage of each element. It clearly shows that the Cu-BTC MOF is composed of three elements as expected: C, O and Cu. The ratio among the elements approximately confirms the molecular formula of Cu-BTC ($C_{18}H_6Cu_3O_{12}$).

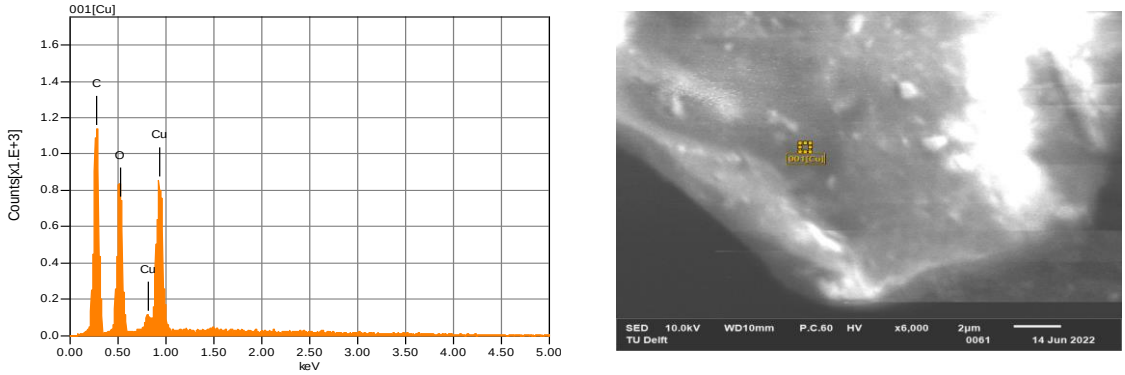

Figure 19: EDS spectrum of Cu-BTC sample.

Formula	Atom%
C	62.08
O	28.33
Cu	9.58
Total	100

Table 2: elemental composite of Cu-BTC.

Additionally, EDS mapping was performed to further testify the elemental composition of pyramidal shaped crystals (figure 20). As it is shown in figure 20, the crystal mainly consists of Cu and O where carbon mainly comes from the substrate. This further confirms the presence of metal oxide by-products which formed during the synthesizing process.

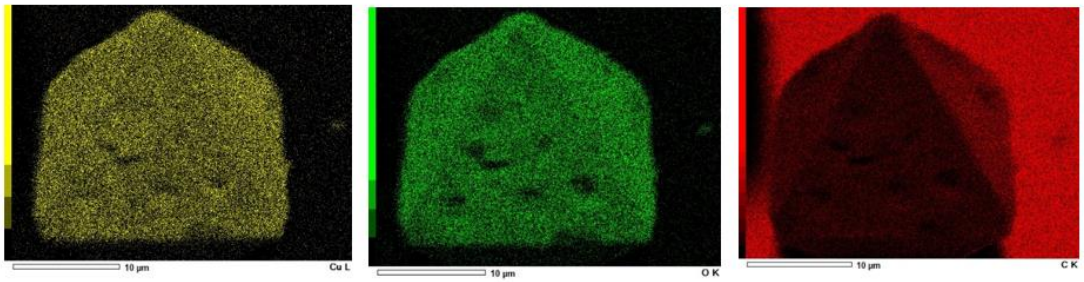

Figure 20: EDS mapping of element distribution in pyramidal shaped crystal.

Cu-HAB

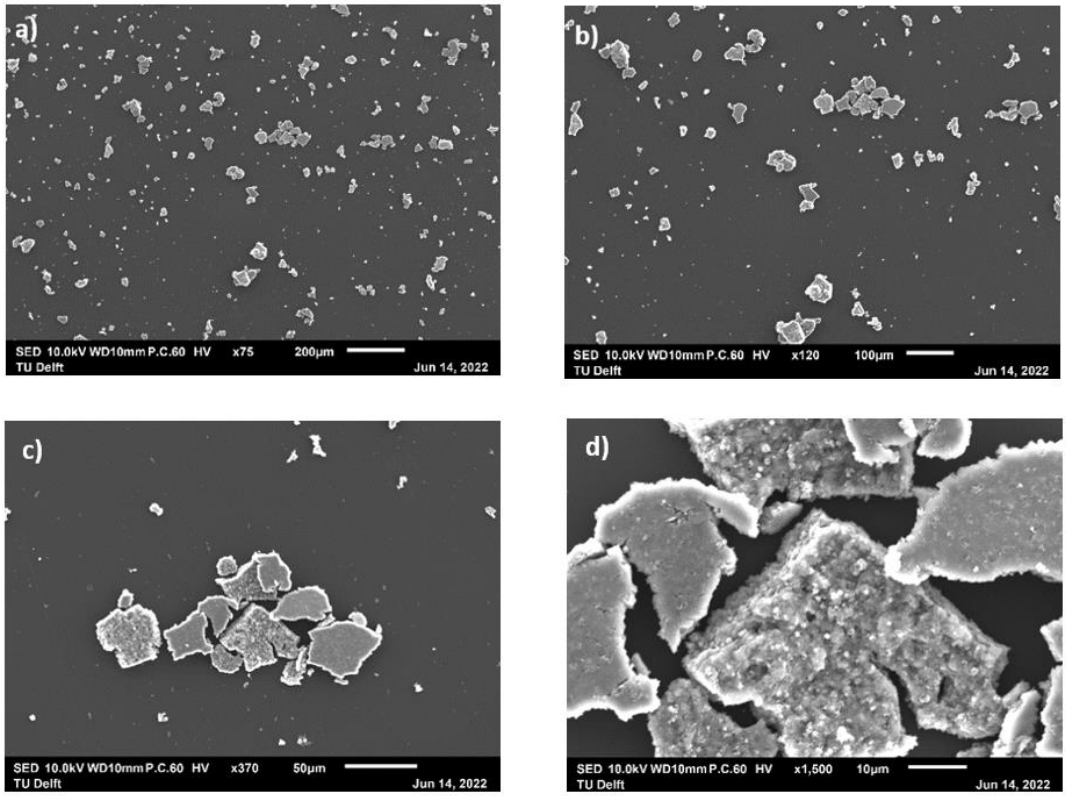

Figure 21: SEM images of Cu-HAB sample. The scale bar corresponds to 200 µm for (a), 100 µm for (b), 50 µm for (c) and 10 µm for (d).

Figure 21 shows SEM graph of Cu-HAB sample. Cu-HAB shows 2D honeycomb structure composed of aggregated small particles in nano scale which is highly porous (figure 21d) [33]. Moreover, from the EDS result (Figure 22 and table 3), it is clear that the main elements present in the MOF structure are C, N and Cu, as expected. The atom percentages of C and N are almost the same which confirms the chemical formula of Cu-HAB ($Cu_3(C_6N_6H_6)_2$). The excessive Cu element and O are from copper oxide by-products. And a small amount of Cl is detected which comes from HAB precursor.

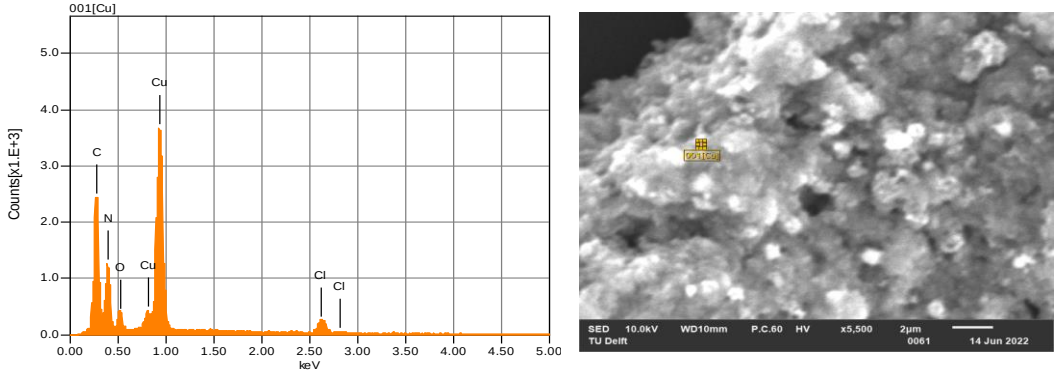

Figure 22: EDS spectrum of Cu-HAB sample.

Formula	Atom%
C	29.45
N	29.78
Cu	17.65
O	19.74
Cl	3.38
Total	100

Table 3: elemental composite of Cu-HAB.

Cu-HHTP

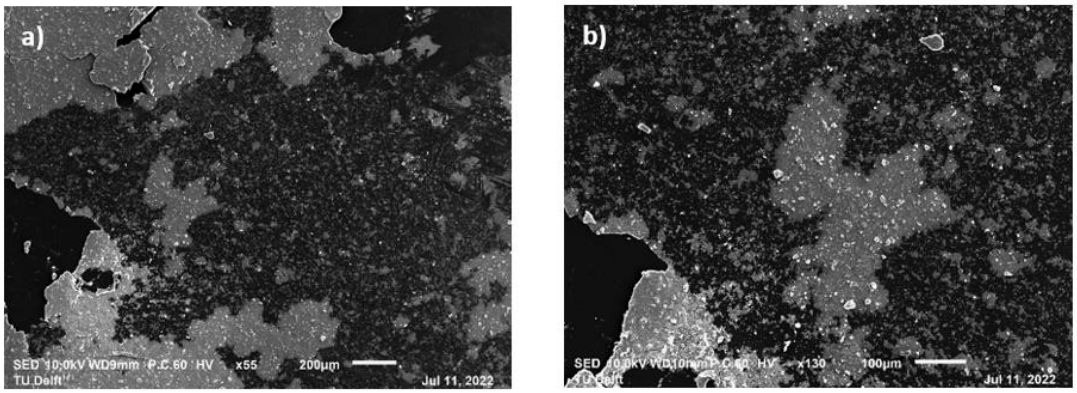

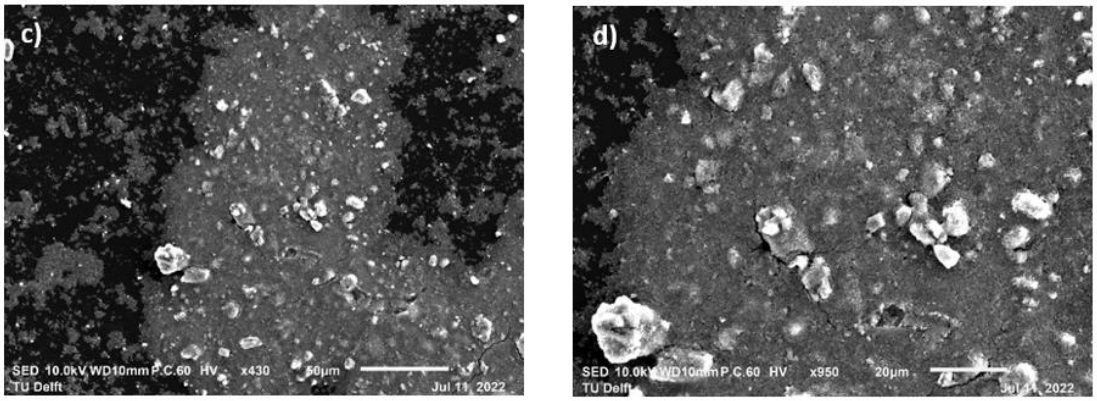

Figure 23: SEM images of Cu-HHTP sample. The scale bar corresponds to 200 µm for (a), 100 µm for (b), 50 µm for (c) and 10 µm for (d).

Figure 23 shows surface morphology of Cu-HHTP in different resolutions. From enlarged SEM graph, many nanometer pores can be observed inside 2D honeycomb structure. The whole structure is highly porous and crystalline [36]. The EDS results (figure 24) further testify the presence of C, Cu and O elements. Also, the atom percentage between C, Cu and O is 70.12%, 21.22% and 8.67% which basically confirms the theorical atom ratio of Cu-HHTP ($C_{36}H_{12}O_{12}Cu_3$) with copper oxide by-product.

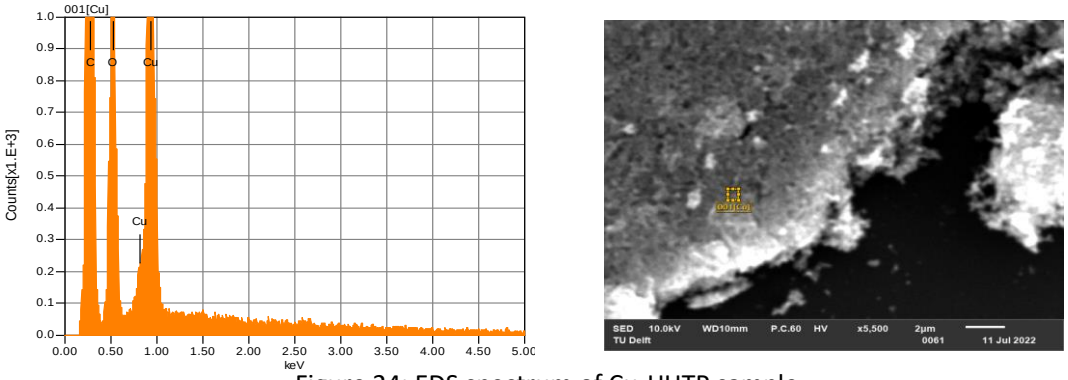

Figure 24: EDS spectrum of Cu-HHTP sample.

Formula	Atom%
C	70.12
O	21.22
Cu	8.67
Total	100

Table 4: elemental composite of Cu-HHTP.

4.1.2 FTIR

Cu-BTC

FTIR analysis was conducted to observe the function groups of samples. As shown in figure 25, the broad bonds at 3700-4000 cm^{-1} come from the vibration of O-H bond due to the absorption of water. Then the strong peaks at 1373, 1430 and 1681 cm^{-1}

are attributed to carboxylate (COOH) groups in BTC. Due to the binding of COOH groups and Cu ions, asymmetric, symmetric types of C=O and C-O stretching can be found in the spectrum. Besides, the peak at about 659 cm^{-1} is from metal-oxide bond which is Cu-O here. The whole spectrum is consisted with the previous results reported [29].

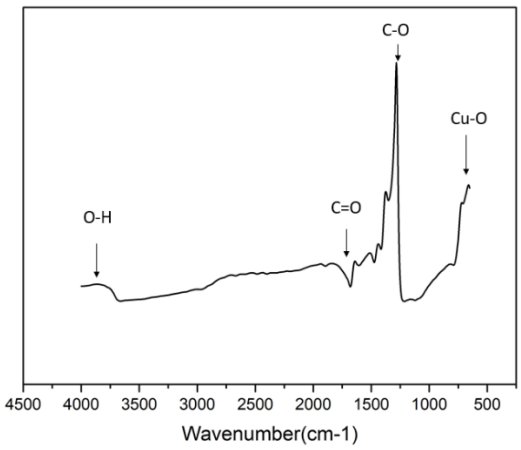

Figure 25: FTIR spectrum of Cu-BTC sample.

Cu-HAB

Next, figure 26 shows the FTIR spectrum of Cu-HAB sample. Similarly, the peaks around 3700 cm^{-1} comes from O-H bond in water. And the peak at 3066 cm^{-1} is due to the N-H bond which is from HAB linker. The strong peak at 2356 cm^{-1} is attributed to CO_2 molecule from air. The next peak observed at 1596 cm^{-1} is caused by the stretching of C=C double bond from central benzene core of HAB ligand. The high intensity peak at 1249 cm^{-1} corresponds to the stretching vibration of C-H. And Cu-N stretching leads to the peak around 990 cm^{-1} which further confirms the coordination between Cu and HAB ligands. In the last, the existence of copper oxide leads to the stretching of Cu-O at 756 cm^{-1}.

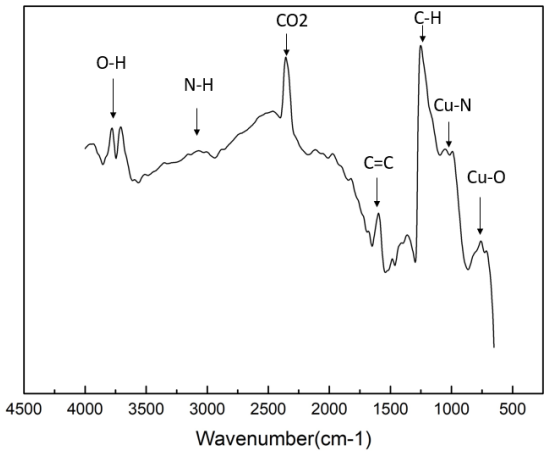

Figure 26: FTIR spectrum of Cu-HAB sample.

Cu-HHTP

Figure 27 represents FTIR results of Cu-HHTP. The strong peak around 3600-3900 cm^{-1} is contributed to the stretching of O-H bond. C-H bond in the benzene ring causes the peak at around 3200 cm^{-1}. And CO_2 from air causes the strong absorption band at 2360 cm^{-1}. The peak at 1596 cm^{-1} is due to C=C bond in aromatic ring. And the peaks around 960 cm^{-1} correspond to C-O stretching. In the last, Cu-O peak can be found at 709 cm^{-1}.

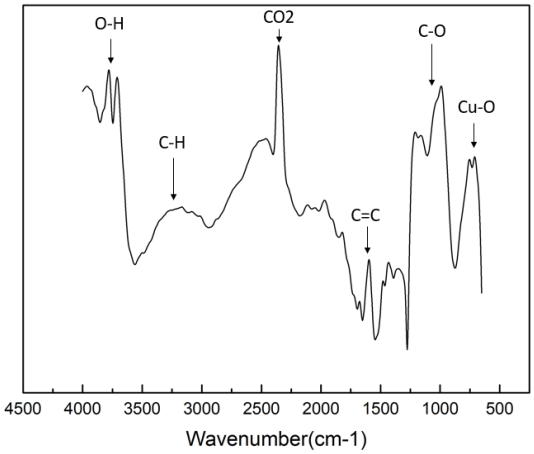

Figure 27: FTIR spectrum of Cu-HHTP sample.

4.2 Electrochemical measurements

After analyzing the surface morphology and bond structure of samples, a series of electrochemical measurements were done to better investigate catalytic activity, electrical conductivity, and stability of Cu-BTC, Cu-HAB and Cu-HHTP. The following content is focused on the results from LSV, CV, EIS and CA measurements of each MOF.

4.2.1 LSV and CV results

Cu-BTC

The electrochemical CO_2 reduction was first studied by LSV and CV in 1M $KHCO_3$ electrolyte. The results are shown in figure 28, where the red line represents the experiment performed in CO_2 saturated solution and the black line represents the experiment performed in N_2 saturated solution.

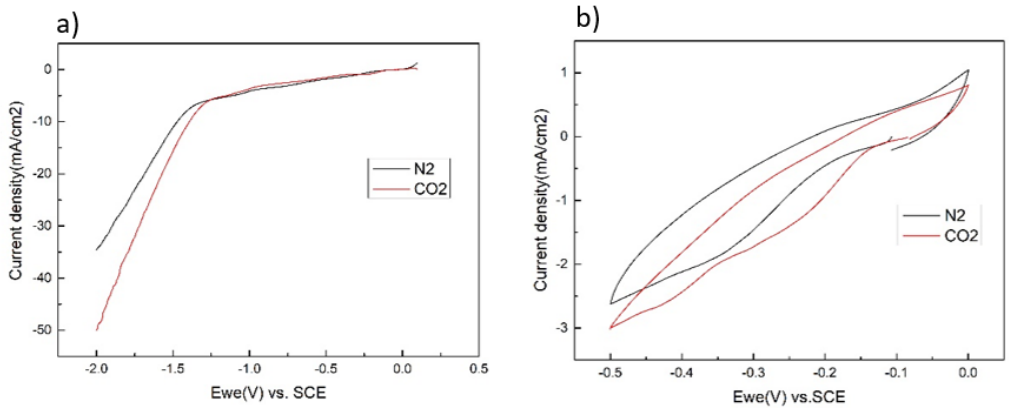

Figure 28: The a) LSV and b) CV curves of Cu-BTC sample in CO_2 and N_2 saturated electrolyte with scan rates of 50 mV/sec and 100 mV/sec, respectively.

From the LSV curves, it can be observed that Cu-BTC in CO_2 saturated solution has higher current densities and lower onset potential than in N_2 saturated solution. This shift in onset potential can be due to the additional CO_2 conversion reactions occurring in CO_2 saturated solution which requires less potential compared to HER in N_2 saturated solution [56]. The reduction current density increases sharply in N_2 and CO_2 saturated electrolyte, at around -1.4V vs SCE. As can be seen in figure 28a, at potentials higher than -1.4 V, the current density in CO_2 saturated electrolyte is observably higher than in N_2 saturated electrolyte. For instance, the maximum current density measured in CO_2 saturated solution reaches at -50 mA/cm^2 at -2V vs SCE, while the maximum current density in N_2-saturated solution is around -35 mA/cm^2 at the same potential. The reason behind this observation can be related to the fact that in the case of N_2-saturated electrolyte, the increase in current density is only due to the electrolysis of water, while the increases in current density in saturated-state of CO_2 is the result of the joint reaction of HER and CO_2 reduction. Therefore, it can be concluded that Cu-BTC sample has a certain electrocatalytic activity towards CO_2 reduction.

Additionally, CV results were recorded in the range of -0.5V to 0V for Cu-BTC sample. The shape of CV curves in CO_2 and N_2 saturated solution are similar but the current density of CO_2 saturated sample is higher. Besides, the CV curves show satisfying capacitance activity of Cu-BTC due to its porous structure as expected.

Cu-HAB

Next, the LSV and CV results for Cu-HAB MOF can be found in figure 29. From LSV results, significant difference is not observed in in N_2 and CO_2 saturated electrolyte which can be duo to a low selectivity of this sample towards CO_2RR. The onset potentials in both cases are around -1.2V, after which the reduction current densities increase rapidly. The maximum current density of Cu-HAB reaches to –75 mA/cm^2 which is a result of high catalytic activity of Cu-HAB. From CV curves, reduction and oxidation peaks can be observed, occurring in both N_2 and CO_2 saturated electrolyte. Also, the peak separation between oxidation and reduction peaks is relatively small (around 100mV) which indicates the reaction can be reversible redox of HAB molecule [33]. Moreover, higher surface area of the CV curves in case of Cu-HAB rather than Cu-BTC, shows higher capacitive activity and porosity of this material, which has been already observed in SEM figures.

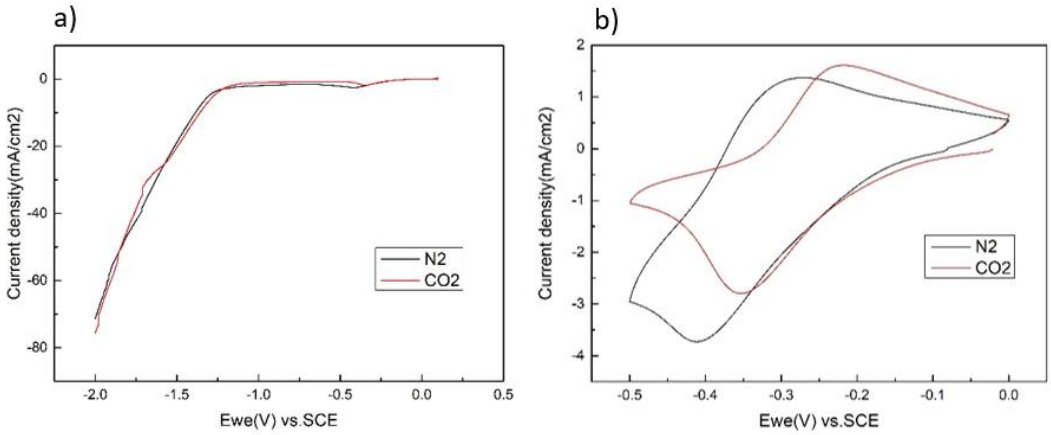

Figure 29: The a) LSV and b) CV curves of Cu-HAB sample in CO_2 and N_2 saturated electrolyte.

Cu-HHTP

Finally, figure 30 shows the LSV and CV curves of Cu-HHTP sample. Similar with Cu-BTC, Cu-HHTP shows lower onset potential and higher current densities in CO_2 saturated electrolyte compared to N_2. It can be seen that the onset potential for the sample in N_2 saturated solution is over -1.3V, while it in CO_2 saturated solution is only around -1.1V vs. SCE. In addition, the LSV curves show significant difference in the current densities of different electrolytic media. Maximum current density of the cell in CO_2 saturated solution reaches to -64 mA/cm^2, however, in N_2 saturated solution it only goes up to -36 mA/cm^2. This can be an indication of the occurrence of CO_2RR which needs further investigation. On the other hand, from the large area of CV curves, high capacitance of Cu-HHTP can be concluded which is consistent with what was observed in SEM figures.

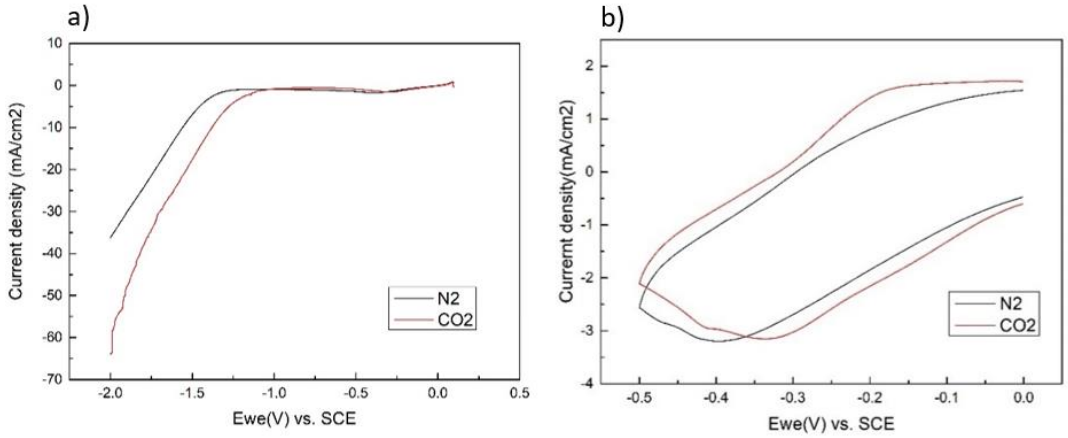

Figure 30: The a) LSV and b) CV curves of Cu-HHTP sample in CO_2 and N_2 saturated electrolyte.

Comparison between three MOFs

To better compare and analyze the electrochemical performance of different MOF samples, figure 31 shows the LSV and CV curves for all three MOF catalysts in CO_2 saturated electrolyte. Overall, Cu-HAB shows the highest current densities while Cu-BTC is the lowest one. The reason behind it could be duo to the large amount of exposed active sites of 2D MOFs compared to 3D ones [33]. Moreover, from the range of measured current density in the case of these three MOFs, it can be concluded that 2D MOFs show higher catalytic activity and charge transfer ability rather than the 3D MOF. Additionally, in the context of 2D MOFs, since Cu-HAB has a smaller organic ligand, a denser active sites and higher catalytic activity is expected, in comparison with Cu-HHTP [33]. On the other hand, it's obvious that the areas of CV curves for 2D MOFs are much larger than Cu-BTC which indicates that 2D MOFs show much higher capacitance activity than Cu-BTC benefiting from their 2D porous structure.

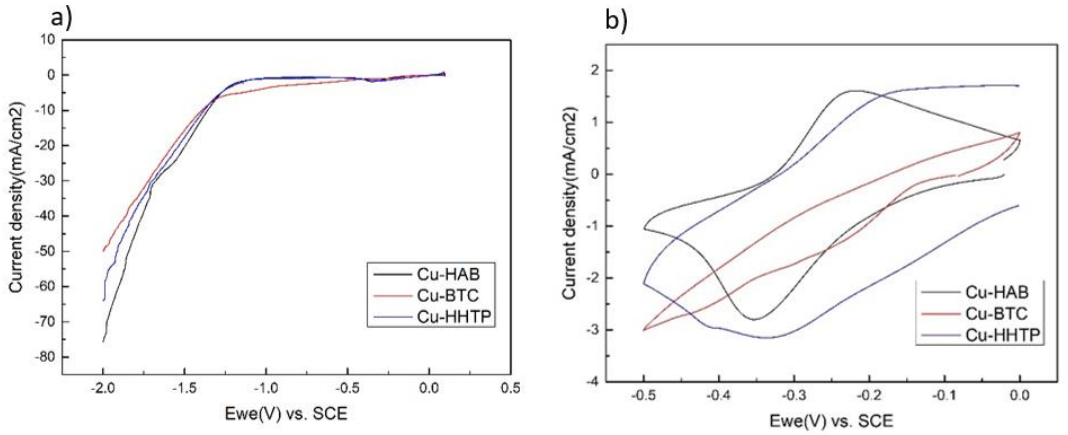

Figure 31: The a) LSV and b) CV curves of Cu-BTC, Cu-HAB and Cu-HHTP samples in CO_2 saturated electrolyte.

4.2.2 EIS results

In this section, to further analyze the catalytic and electrical properties of the samples, EIS measurement was performed. The results for all three samples can be found in figure 32. During the electrochemical process on the surface of the electrode, reaction kinetic is determined by R_{ct} which is presented by the diameter of semicircle as explained in section 3. A smaller R_{ct} value means faster kinetics and better electrical conductivity.. From figure 32d, it can be concluded that Cu-HAB has the smallest value of R_{ct}, followed by Cu-HHTP, and Cu-BTC. This result further testifies the higher electron transfer rate between interface and electrolyte, and better electrical conductivity of 2D MOFs.

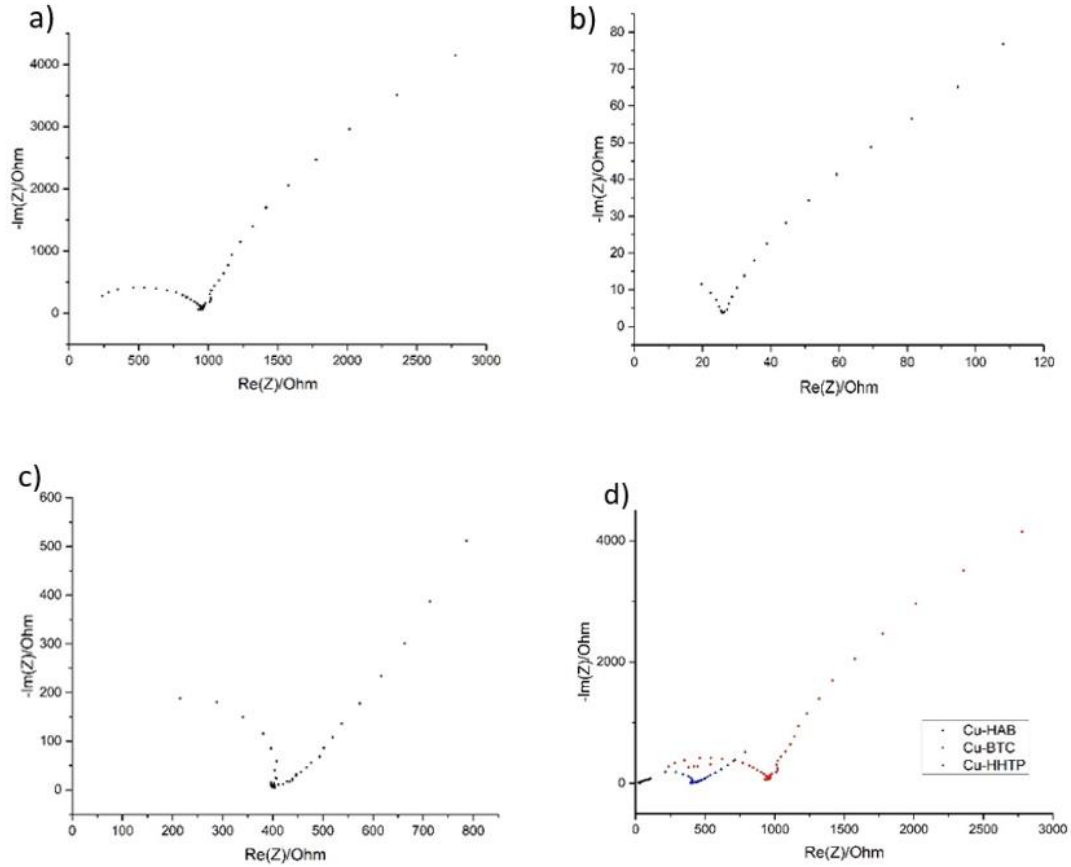

Figure 32: The EIS results for a) Cu-BTC, b) Cu-HAB, c) Cu-HHTP, d) overall for all three MOFs.

4.2.3 CA results

Stability is also an important performance indicator for catalyst selection. The electrocatalytic stability can be determined by CA measurement conducted in a certain period of time. The CA measurement presented in figure 33 was performed under a constant potential of -1.6V (vs Ag/AgCl) for 60 minutes. As can be observed, there is a current drop soon after the start of reaction which is due to the formation of intermediates [57]. After that, current keeps relatively stable and only has a small attenuation for all three samples which can be a result of their high stability within the

operating conditions of the measurements. Though, it is also been stated in the literature that Cu-O_4 sites can be converted to CuO_x species during CO_2RR process which might be the reason behind current degradation of Cu-HHTP [36].
Additionally, It can be observed that Cu-HAB has the highest current densities, followed by Cu-HHTP, and Cu-BTC . The result is further confirms our observations from LSV results measured before.

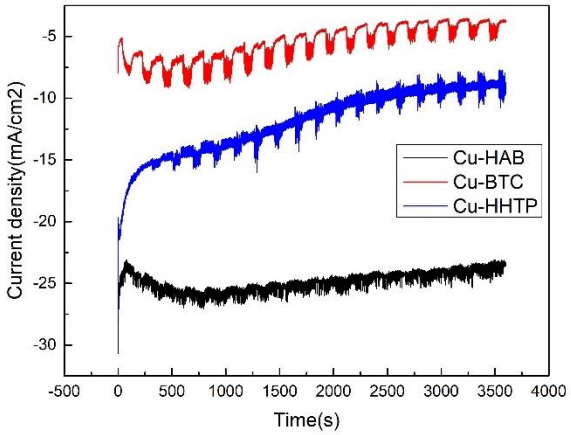

Figure 33: The CA results for Cu-HAB, Cu-BTC, Cu-HHTP samples at -1.6V vs Ag/AgCl.

4.3 Product analysis

Next, to better analyze product selectivity of 2D MOFs, GC and NMR were used to detect and quantify gas and liquid products, respectively.

4.3.1 GC

First, GC measurements were performed to investigate the gaseous product selectivity of 2D MOFs in 1M $KHCO_3$ under a constant potential of -1.6 V (vs Ag/AgCl) for 60 minutes. The main CO_2RR product detected for all the samples are CH_4 and C_2H_4. The average faraday efficiency of each product is calculated and shown in figure 34.

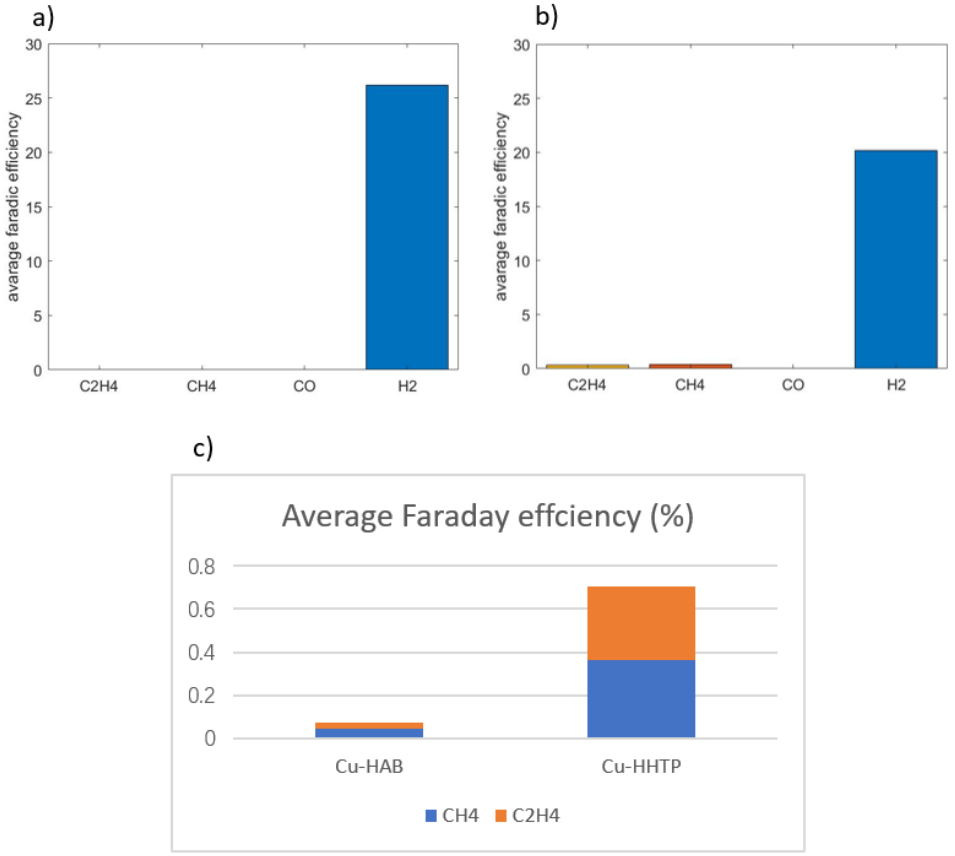

Figure 34: The average FEs calculated a) Cu-HAB, b) Cu-HHTP samples and c) gas products of two MOFs.

From GC results, it is clear that Cu-HHTP performs best in terms of CO_2 conversion to CH_4 and C_2H_4. Though the calculated FEs for CH_4 and C_2H_4 are not high enough in comparison with previous studies on 2D MOFs [36]. There are few reasons that might cause this incompatibility with literature namely; concentration of CO below 1000 ppm is challenging to be detected by the detectors in GC device which may cause some loss of FE. Also, n-butane has been detected by the thermal conductivity detector in all of the experiments. However, FE of n-butane has not been calculated in this report due to the lack of calibration. On the other hand, the GC cell has higher electrode surface to electrolyte volume ratio than normal three-electrode flow cells which can deplete dissolved CO_2 faster. This may cause some difficulties in maintaining the saturation of CO_2 within the flow cell and lead to lower FEs of products.
Overall, the GC results are consistent with previous LSV results. Since LSV curves of Cu-HAB (figure 29) show little difference between CO_2 and N_2 saturated systems, the product selectivity of it considered not to be satisfying. The reason behind this can be due to the fact that Cu species in Cu–N_4 sites are more difficult to be reduced compared with those in Cu–O_4 sites and the adsorption of CO_2 in Cu-N_4 sites is not strong enough [36]. Although, higher current densities and electrical conductivity of HAB-based MOF concludes high-efficient electron transfer in Cu-N_4 bonding rather than Cu-O_4.

4.3.2 NMR

NMR analysis were used to further detect liquid products of samples. Figure 35 shows the NMR results of Cu-HAB and Cu-HHTP. It can be observed that the main liquid products detected are formic acid, ethyl acetate, acetaldehyde, ethanol and propionaldehyde. Also, a small amount of methanol is detected in Cu-HHTP sample (0.2% FE). The total FE of liquid products in Cu-HHTP sample reaches 47.9%, which is much higher than Cu-HAB sample (15.4%). This further proves that Cu-O_4 sites may perform better in adsorption and conversion of CO_2 molecules than Cu-N_4 sites.

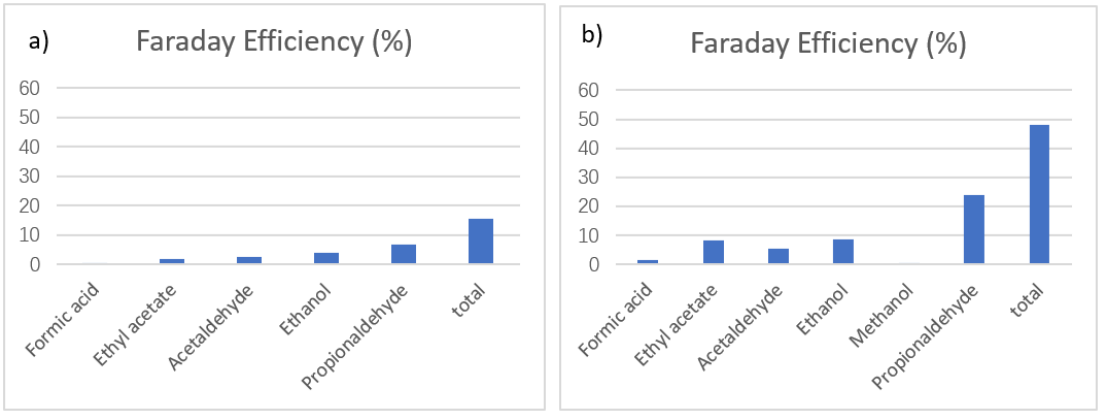

Figure 35: The average FEs of liquid products for a) Cu-HAB and b) Cu-HHTP samples.

5

Conclusion

In summary, the thesis aims to investigate the electrocatalytic performance of three kinds of Cu-based MOFs for CO_2RR: Cu-BTC, Cu-HAB and Cu-HHTP, where Cu-BTC is a conventional 3D MOF and the other two are 2D MOFs. The surface morphology, electrochemical performance of each MOF was researched during this project. In addition, the product selectivity of 2D MOFs was further studied to find their potential as CO_2RR catalysts. From the results, it was observed that 2D MOFs show better catalytic activity, conductivity, and higher surface area (as we could see in CV curves) compared to conventional 3D MOFs, because of their higher porosity and exposure active sites. Especially, Cu-HAB shows best conductivity and catalytic activity (-80 mA/cm^2), due to the presence of Cu-N coordination in the MOF structure as well as smaller organic linker. However, Cu-HHTP shows higher product selectivity towards gas and liquid products than Cu-HAB due to the fact that $Cu\text{-}O_4$ can engage with CO_2 molecule better and achieve higher FE.

6

Future Outlook

During the experiments, some limitations such as low solubility of CO_2 can be further improved to enhance the accuracy of experiments. In this section, several strategies and recommendations are proposed as references for future study.

(1) In order to improve the accuracy of basic electrochemical measurements, a two-compartment three electrode system can be designed with a fixed position for working electrode, reference electrode and counter electrode. In this way, consistency of different trials can be better achieved. Also, the stability and reliability of the experiments can be improved.

(2) Gas diffusion electrode can help with enhancing CO_2 solubility and achieve higher FEs. Using gas diffusion electrodes can increase the exposure surface area of the catalyst directly to CO_2 molecules which can further improve the production efficiency.

(3) On the other hand, the FEs of different products can change a lot under different potential range. Potential dependency of FE can be further investigated to better understand catalytic process of the materials.

(4) In addition, electrolyte plays an important role during electrocatalytic process.

The concentration, species and PH value can influence the local reaction conditions and product distribution largely. Therefore, the catalytic performance of materials could be improved by adjusting the concentration and type of electrolytes.

A

Appendix: GC Calibration

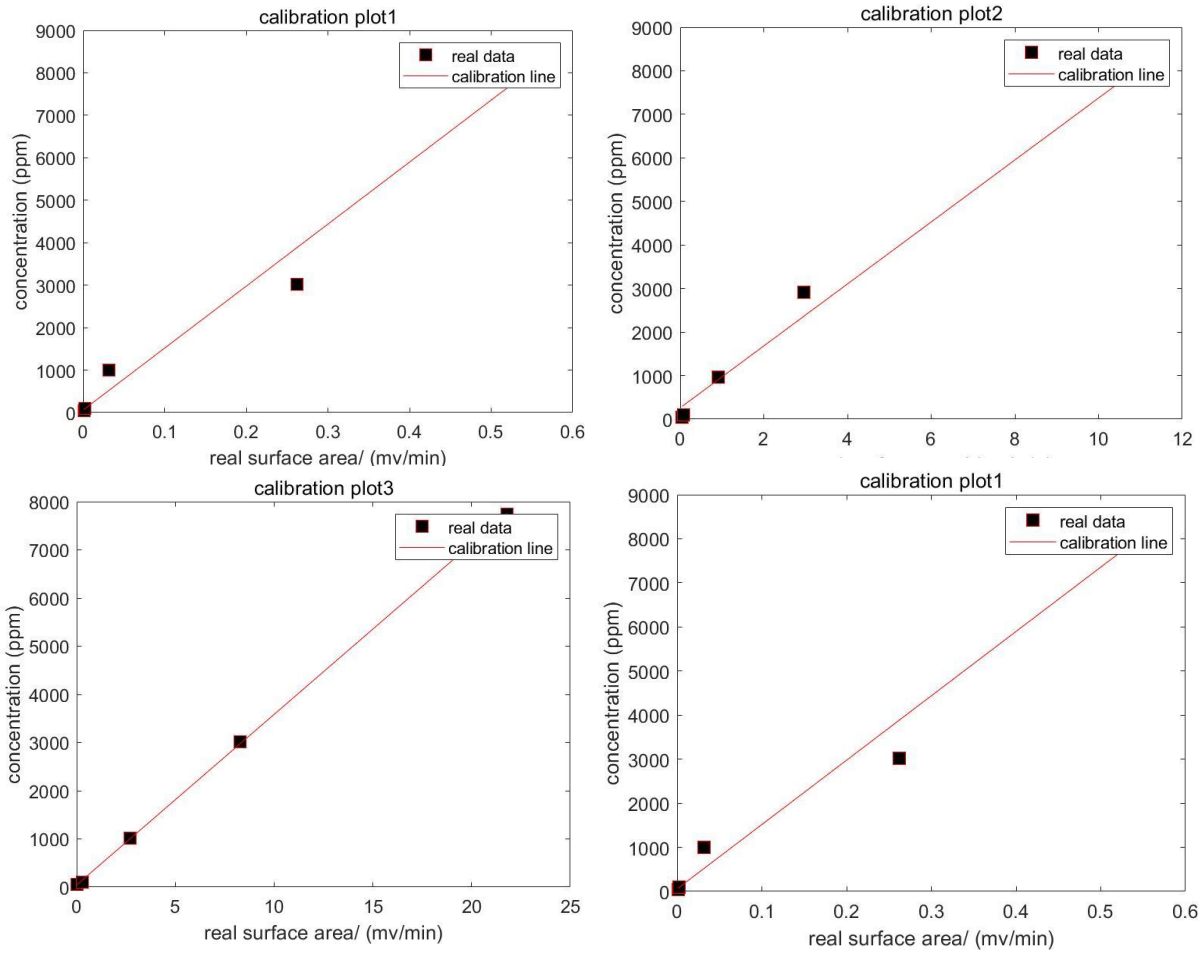

Figure A.1: Calibration plots for a) H_2, b) CH_4, c) C_2H_4, d) CO.

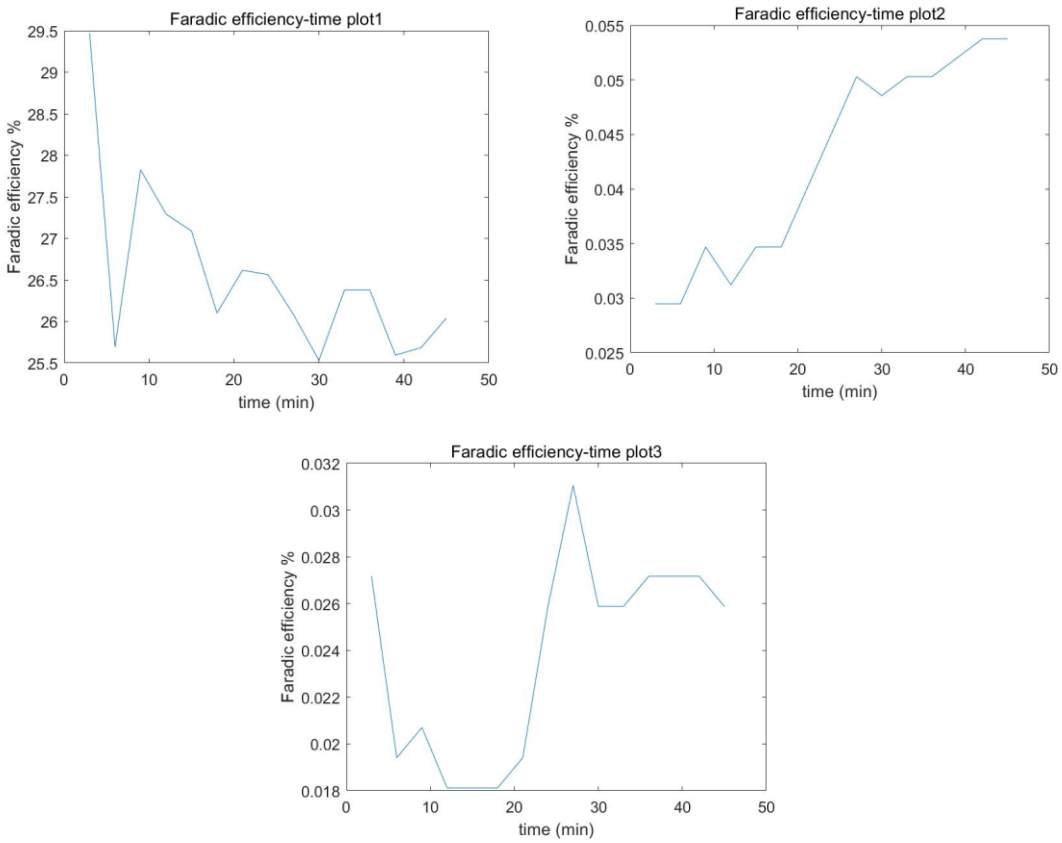

Figure A.2: FE-time plot of a) H_2, b) CH_4, c) C_2H_4 product for Cu-HAB sample.

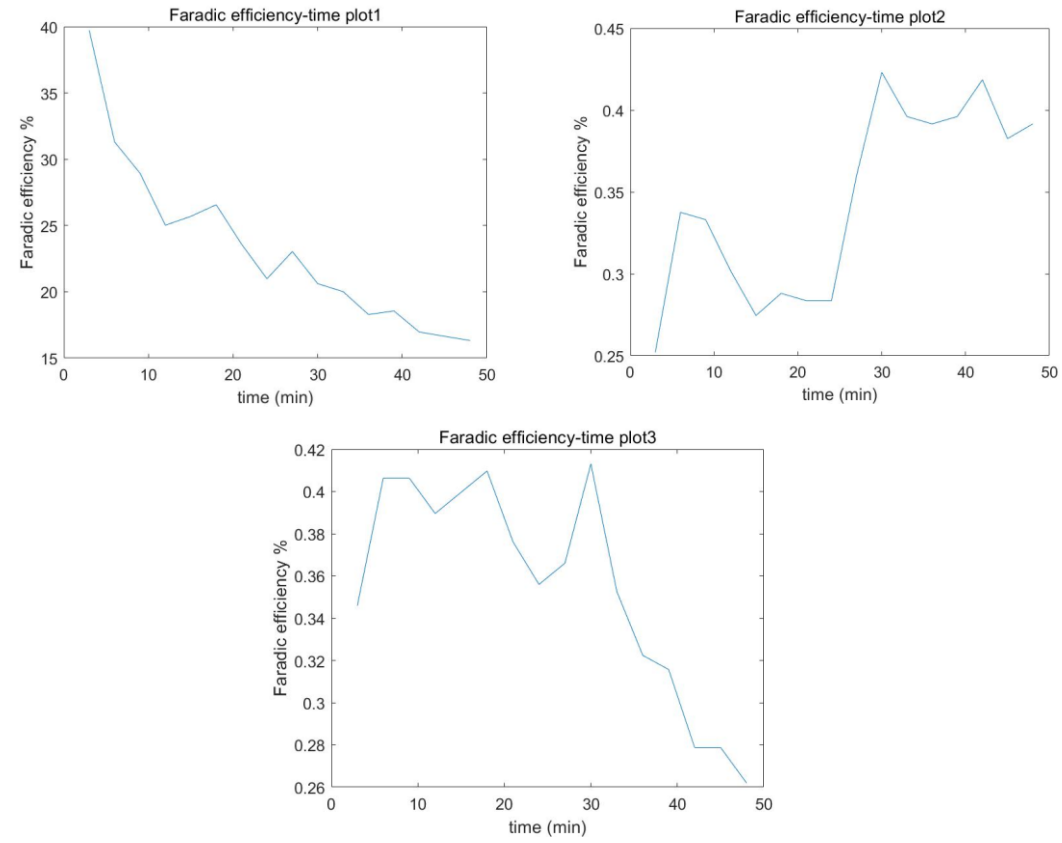

Figure A.3: FE-time plot of a) H_2, b) CH_4, c) C_2H_4 product for Cu-HHTP sample.

Reference

[1] S. S. A. Shah, T. Najam, M. Wen, S. Zhang, A. Waseem, H. Jiang. "Metal–Organic Frameworks for Electrocatalytic Reduction of Carbon Dioxide" *American Chemical Society*, 2015, 137: 14129–14135, https://doi.org/10.1021/jacs.5b08212

[2] W. A. Hika, A. R. Woldu, "The impact of anode materials on the performance of electrochemical CO2 reduction to carbon monoxide", *SN Applied Sciences*, 2021, 3: 812, https://doi.org/10.1007/s42452-021-04796-x

[3] Q. Qin, M. Sun, G. Wu, L. Dai, ""Emerging of heterostructured materials in CO_2 electroreduction: A perspective", *Carbon Capture Science & Technology*, 2022, 3: 100043, https://doi.org/10.1016/j.ccst.2022.100043

[4] Z. Sun, T. Ma, H. Tao, Q. Fan, B. Han, "Fundamentals and Challenges of Electrochemical CO2 Reduction Using Two-Dimensional Materials", *Chemistry*, 2017, 3: 560-587, https://doi.org/10.1016/j.chempr.2017.09.009

[5] F. N. Al-Rowaili, A. Jamal, M. S. Ba-Shammakh, A. Rana, "A Review on Recent Advances for Electrochemical Reduction of Carbon Dioxide to Methanol Using Metal–Organic Framework (MOF) and Non-MOF Catalysts: Challenges and Future Prospects", *ACS Sustainable Chemistry & Engineering*, 2018, 6: 15895-15914, http://dx.doi.org/10.1021/acssuschemeng.8b03843

[6] J. Liu, D. Yang, Y. Zhou, G. Zhang, G. Xing, Y. Liu, Y. Ma, O. Terasaki, S. Yang, L. Chen, "Tricycloquinazoline Based 2D Conductive Metal-Organic Frameworks as Promising Electrocatalysts for CO_2 Reduction", *Angewandte Chemie*, 2021, 133: 14594-14600, https://doi.org/10.1002/ange.202103398

[7] X. Zhang, S. Guo, K. A. Gandionco, A. M. Bond, J. Zhang, "Electrocatalytic carbon dioxide reduction: from fundamental principles to catalyst design", *Materials Today Advances*, 2020, 7: 100074, https://doi.org/10.1016/j.mtadv.2020.100074

[8] W. Zhang, Y. Hu, L. Ma, G. Zhu, Y. Wang, X. Xue, R. Chen, S. Yang, Z. Jin, "Progress and Perspective of Electrocatalytic CO2 Reduction for Renewable Carbonaceous Fuels and Chemicals", *Advanced Science*, 2017, 5: 1700275, https://doi.org/10.1002/advs.201700275

[9] M. B. Ross, P. D. Luna, Y. Li, C. T. Dinh, D. Kim, P. Yang, E. Sargent, "Designing materials for electrochemical carbon dioxide recycling", *Nature Catalysis*, 2019, 2: 648-658, https://doi.org/10.1038/s41929-019-0306-7

[10] R. Lin, J. Guo, X. Li, P. Patel, A. Seifitokaidani, "Electrochemical Reactors for CO_2 Conversion", *Catalysts*, 2020, 10:473, https://doi.org/10.3390/catal10050473

[11] M. A. Tekalgne, H.H Do, A. Hasani, Q. Le, H. Jang, S. H. Ahn, S. Y. Kim," Two-dimensional materials and metal-organic frameworks for the CO_2 reduction reaction", *Materials Today Advances*, 2020, 5: 100038, https://doi.org/10.1016/j.mtadv.2019.100038

[12] Y. Pei, H. Zhong, F. Jin, "A brief review of electrocatalytic reduction of CO_2 — Materials, reaction conditions, and devices.", *Energy Science & Engineering*, 2021, 9: 1012-1032, https://doi.org/10.1002/ese3.935

[13] E. Tayyebi, J. Hussain, Y. Abghoui, E. Skulason, "Trends of Electrochemical CO_2 Reduction Reaction on Transition Metal Oxide Catalysts", *The Journal of Physical Chemistry*, 2018, 122: 10078-10087, https://doi.org/10.1021/acs.jpcc.8b02224
[14] A. Handoko, C. Ong, Y. Huang, Z. Lee, L. Lin, G. Panetti, Y. Boon, "Mechanistic Insights into the Selective Electroreduction of Carbon Dioxide to Ethylene on Cu_2O-Derived Copper Catalysts", *Physical Chemistry*, 2016, 120: 20058-20067, https://doi.org/10.1021/acs.jpcc.6b07128
[15] A.K. Geim, K.S. Novoselov, "The rise of graphene", *a Collection of Reviews from Nature Journals*, 2010, 6: 183-191, https://doi.org/10.1142/9789814287005_0002
[16] J. Wu, R. M. Yadav, M. Liu, P. Sharma, C. Tiwary, L. Ma, X. Zou, X. Zhou, B. Yakobson, J. Lou, P. Ajayan, "Achieving Highly Efficient, Selective, and Stable CO_2 Reduction on Nitrogen-Doped Carbon Nanotubes", *ACS nano*, 2015, 9: 5364-5371, https://doi.org/10.1021/acsnano.5b01079
[17] L. Ma, Y. Li, Y. Xu, J. Sun, T. Wu, X. Ding, Y. Niu, "Two-dimensional transition metal dichalcogenides for electrocatalytic nitrogen fixation to ammonia: Advances, challenges and perspectives", *Electrochemistry Communications*, 2021, 125: 107002, https://doi.org/10.1016/j.elecom.2021.107002
[18] M. Zeng, Y. Li, "Recent Advances in Heterogeneous Electrocatalysts for Hydrogen Evolution Reaction", *Materials Chemistry A*, 2015, 3: 14942-14962, https://doi.org/10.1039/C5TA02974K
[19] S. Francis, J. Velazquez, L. Ferrer et al. "Reduction of Aqueous CO_2 to 1-Propanol at MoS_2 Electrodes", *Chemistry of Materials*, 2018, 30: 4902-4908, https://doi.org/10.1021/acs.chemmater.7b04428
[20] D. D. Medina, A. Mahringer, T. Bein, "Electroactive Metalorganic Frameworks", *Israel Journal of Chemistry*, 2018, 58: 1089-1101, https://doi.org/10.1002/ijch.201800110
[21] R. Wang, F. Kapteijn, J. Gascon, "Engineering Metal-Organic Frameworks for the Electrochemical Reduction of CO_2: A Mini-review.", *Chemistry - An Asian Journal*, 2019, 14: 3452-3461, https://doi.org/10.1002/asia.201900710
[22] D. N. Celada, A. S. Varela, "CO_2 electrochemical reduction on metal–organic framework catalysts: current status and future directions", *Material Chemistry A*, 2022, 10: 5899-5917, https://doi.org/10.1039/D1TA10440C
[23] J. Liu, D. Yang, Y. Zhou, G. Zhang, G. Xing, Y. Liu, Y. Ma, O. Terasaki, S. Yang, L. Chen, "Tricycloquinazoline Based 2D Conductive Metal-Organic Frameworks as Promising Electrocatalysts for CO2 Reduction", *Angewandte Chemie*, 2021, 60: 14473-14479, https://doi.org/10.1002/anie.202103398
[24] L. Majidi, A. Ahmadiparidari, N. Shan, S. Misal, K. Kumar, Z. Huang, S. Rastegar, Z. Hemmat, X. Zou, P. Zapol, J. Cabana, L. Curtiss, A. S. Khojin, "D Copper Tetrahydroxyquinone Conductive Metal–Organic Framework for Selective CO2 Electrocatalysis at Low Overpotentials", *Advanced Materials*, 2021, 33: 2004393, https://doi.org/10.1002/adma.202004393
[25] A. R. Bagheri, M. Ghaedi, "Application of Cu-based metal-organic framework (Cu-BDC) as a sorbent for dispersive solid-phase extraction of gallic acid from orange

juice samples using HPLC-UV method", *Arabian Journal of Chemistry*, 2020, 13: 5218-5228, https://doi.org/10.1016/j.arabjc.2020.02.020

[26] A. Jonathan, V. Daniel, B. Garikoitz, C. Oscar, C. Pedro, I. Angel, "Copper-Based Metal–Organic Porous Materials for CO_2 Electrocatalytic Reduction to Alcohols", *chemistry and sustainability, energy and materials*, 2017, 10: 1100-1109, https://doi.org/10.1002/cssc.201600693

[27] J. F. Kurisingal, Y. Rachuri, Y. Gu, G. H. Kim, D. W. Park, "Binary metal-organic frameworks: Catalysts for the efficient solvent-free CO_2 fixation reaction via cyclic carbonates synthesis", *Applied Catalysis A: General*, 2019, 571: 1-11, https://doi.org/10.1016/j.apcata.2018.11.035

[28] S. N. Nobar, "Cu-BTC synthesis, characterization and preparation for adsorption studies", *Materials Chemistry and Physics*, 2018, 213: 343-351, https://doi.org/10.1016/j.matchemphys.2018.04.031

[29] R. Nivetha, A. Sajeev, A. Paul, K. Gothandapani, S. Gnanasekar, P. Bhardwaj, G. Jacob, R. Sellappan, V. R, K.C.N. Raja, P. Sudhagar, S. Jeong, A. Grace, "Cu based Metal Organic Framework (Cu-MOF) for electrocatalytic hydrogen evolution reaction.", *Materials Research Express*, 2020, 7: 114001, http://dx.doi.org/10.1088/2053-1591/abb056

[30] T. Khosravi, M. Omidkhah, "Preparation of CO_2 selective composite membranes using Pebax/CuBTC/PEG-ran-PPG ternary system", *Journal of Energy Chemistry*, 2017, 3: 530-539, https://doi.org/10.1016/j.jechem.2016.10.013

[31] J. Kim, H. Y. Cho, W. S. Ahn, "Synthesis and Adsorption/Catalytic Properties of the Metal Organic Framework CuBTC", *Catalysis Surveys from Asia*, 2012, 16: 106-119, https://doi.org/10.1007/s10563-012-9135-2

[32] B. Cui, C. Wang, S. Huang, L. He, S. Zhang, Z. Zhang, M. Du, "Efficient multifunctional electrocatalyst based on 2D semiconductive bimetallic metal-organic framework toward non-Pt methanol oxidation and overall water splitting", *Journal of Colloid and Interface Science*, 2020, 578: 10-23, https://doi.org/10.1016/j.jcis.2020.05.098

[33] D. Feng, T. Lei, M. R. et al, "Robust and conductive two-dimensional metal−organic frameworks with exceptionally high volumetric and areal capacitance", *Nature Energy*, 2018, 3: 30-36, https://doi.org/10.1038/s41560-017-0044-5

[34] M. L. G. Juarez, C. Morales, J. Flege, E. Flores, M. M. Gonzalez, I. Nandhakumar, D. Bradshaw, "unable Carrier Type of a Semiconducting 2D Metal–Organic Framework $Cu_3(HHTP)_2$", *ACS Applied Materials & Interfaces*, 2022, 14: 12404-12411, https://doi.org/10.1021/acsami.2c00089

[35] S. Gu, Z. Bai, S. Majumder, B. Huang, G. Chen, "Conductive metal–organic framework with redox metal center as cathode for high rate performance lithium ion battery", *Journal of Power Sources*, 2019, 429: 22-29, https://doi.org/10.1016/j.jpowsour.2019.04.087

[36] Y. Zhang, L. Dong, S. Li et al, "Coordination environment dependent selectivity of single-site-Cu enriched crystalline porous catalysts in CO_2 reduction to CH_4", *Nature Communications*, 2021, 12: 6390, https://doi.org/10.1038/s41467-021-

26724-8
[37] M. Yao, X. Lv, Z. Fu, W. Li, W. Deng, G. Wu, G. Xu, “Layer-by-Layer Assembled Conductive MOF Nanofilms for Room Temperature Chemoreceptive Sensing”, *Angewandte Chemie*, 2017, 56: 16510-16514, https://doi.org/10.1002/anie.201709558
[38] S. Xu, X. Guo, Z. Qiao, H. Huang, C. Zhong, “Methyl-Shield Cu-BTC with High Water Stability through One-Step Synthesis and In Situ Functionalization”, *Industrial & Engineering Chemistry Research*, 2020, 59: 12451-12457, https://doi.org/10.1021/acs.iecr.0c02156
[39] A. M. Adbel-Aziz, H. H. Hassan, L. H. A. Badr, “Glassy Carbon Electrode Electromodification in the Presence of Organic Monomers: Electropolymerization versus Activation”, *Analytical Chemistry*, 2020, 92: 7947-7954, https://doi.org/10.1021/acs.analchem.0c01337
[40] K. Akhtar, S. Khan, S. Khan, A. M. Asiri, “Scanning Electron Microscopy: Principle and Applications in Nanomaterials Characterization”, *Handbook of Materials Characterization*, 2019, 113-145, https://doi.org/10.1007/978-3-319-92955-2_4
[41] “ENERGY DISPERSIVE X-RAY SPECTROSCOPY (EDS)”, *MATERIALS EVALUATION AND ENGINEERING. INC.* [online], https://www.mee-inc.com/hamm/energy-dispersive-x-ray-spectroscopyeds/
[42] “Fourier-transform infrared spectroscopy”, *WIKIPEDIA* [online], last edited in 2022, https://en.wikipedia.org/wiki/Fourier-transform_infrared_spectroscopy
[43] “Introduction to FTIR Spectroscopy”, *JASCO* [online], 2022, https://jascoinc.com/learning-center/theory/spectroscopy/fundamentals-ftir-spectroscopy/
[44] R. J. Markovich, C. Pidgeon, “Introduction to Fourier transform infrared spectroscopy and applications in the pharmaceutical sciences”, *Pharmaceutical Research*, 1991, 8: 663-675, https://doi.org/10.1023/A:1015829412658
[45] D. Graham, “What Is Cyclic Voltammetry?”, *SOP4CV* [online], https://sop4cv.com/chapters/WhatIsCyclicVoltammetry.html
[46] T. Paschkewitz, “Linear Sweep Voltammetry (LSV)”, *PINE research* [online], last edited in 2020, https://pineresearch.com/shop/kb/software/methods-and-techniques/voltammetric-methods/linear-sweep-voltammetry-lsv/
[47] “Linear sweep voltammetry”, *WIKIPEDIA* [online], last edited in 2020, https://en.wikipedia.org/wiki/Linear_sweep_voltammetry
[48] “Electrochemical Impedance Spectroscopy (EIS)”, *Knowledge base* [online], https://www.palmsens.com/knowledgebase-article/electrochemical-impedance-spectroscopy-eis/
[49] “Basics of Electrochemical Impedance Spectroscopy”, *GAMRY INSTRUMENTS* [online], https://www.gamry.com/application-notes/EIS/basics-of-electrochemical-impedance-spectroscopy/
[50] B. Lu, “electrochemical impedance spectroscopy (EIS)”, *National Materials Corrosion and Protection Data Center* [Online], 2018, https://www.corrdata.org.cn/news/industry/2018-07-18/169643.html
[51] “What is Gas Chromatography?”, *SHIMADZU* [online],

https://www.ssi.shimadzu.com/service-support/faq/gas-chromatography/what-is-gas-chromatography/index.html
[52] J. V. Henshaw, “The Thermal Conductivity Detector”, *LGGC Europe*, 2006, 4: 39-58, https://doi.org/10.1016/S0301-4770(08)60430-3
[53] S. Aryal, “NMR Spectroscopy- Definition, Principle, Steps, Parts, Uses”, *Microbe Notes* [online], 2022, https://microbenotes.com/nuclear-magnetic-resonance-nmr-spectroscopy/
[54] B. Venu, V. Shirisha, B. Vishali, G. Naresh, R. Kishore, I. Sreedhar, A. Venugopal, “A Cu-BTC metal–organic framework (MOF) as an efficient heterogeneous catalyst for the aerobic oxidative synthesis of imines from primary amines under solvent free conditions”, *New Journey of Chemistry*, 2020, 44: 5972-5979, https://doi.org/10.1039/C9NJ05997K
[55] R. Nivetha, A. Sajeev, A. M. Paul, K. Gothandapani, S. Gnanasekar, P. Bhardwaj, G. Jacob, R. Sellappan, V. Raghavan, K. Chandar, S. Pitchaimuthu, S. K. Jeong, A. N. Grace, “Cu based Metal Organic Framework (Cu-MOF) for electrocatalytic hydrogen evolution reaction”, *Material Research Express*, 2020, 7: 114001, https://doi.org/10.1088/2053-1591/abb056
[56] A. Ismail, G. Samu, A. Balog, E. Csapó, C. Janáky, “Composition Dependent Electrocatalytic Behavior of Au–Sn Bimetallic Nanoparticles in Carbon Dioxide Reduction”, *ACS Energy Letters*, 2018, 4: 48-53, https://doi.org/10.1021/acsenergylett.8b01996
[57] T. Noor, M. Ammad, N. Zaman, N. Lqbal, L. Yaqoob, H. Nasir, “A Highly Efficient and Stable Copper BTC Metal Organic Framework Derived Electrocatalyst for Oxidation of Methanol in DMFC Application”, *Catalysis Letters*, 2019, 149: 3312-3327, https://doi.org/10.1007/s10562-019-02904-6